Seismic reliability of structures equipped with LIR-DCFP bearings in terms of superstructure ductility and isolator displacement

SEISMIC RELIABILITY OF STRUCTURES EQUIPPED WITH LIR-DCFP BEARINGS IN TERMS OF SUPERSTRUCTURE DUCTILITY AND ISOLATOR DISPLACEMENT

Gaspar Auad[(a)(b)][1], Paolo Castaldo[(a)], José L. Almazán[(b)]

[(a)] *Department of Structural, Geotechnical and Building Engineering (DISEG); Politecnico di Torino; Turin, Italy*
[(b)] *Department of Structural Engineering; Pontificia Universidad Católica de Chile; Santiago, Chile*

Abstract

This research deals with the seismic reliability of non-linear base-isolated structures equipped with Lateral Impact Resilient Double Concave Friction Pendulum (LIR-DCFP) devices. Specifically, exceeding probabilities within the reference lifetime are assessed with respect to both superstructure ductility and isolator displacement demand. The innovative LIR-DCFP bearing has an improved inner slider with an internal gap and is capable to reduce adverse effects of the lateral impact between the inner slider and the restraining rims. The dynamic behavior of the superstructure is represented by a simplified one-degree-of-freedom model describing its lateral flexibility. The isolation system is characterized by a model based on rigid body dynamics also including the lateral impact behavior. A wide parametric analysis is developed for several system properties considering the friction coefficients as relevant random variables. Different sets of natural seismic records able to match conditional spectra for a site in Riverside (California) were selected to consider the aleatory uncertainties of the seismic input. Incremental dynamic analyses were performed to determine the statistics of significant engineering demand parameters and compute probabilities exceeding specific limit states to define fragility curves. Finally, employing seismic hazard curves, the seismic reliability of isolated structures was evaluated. For increasing values of the internal gap, structures equipped with LIR-DCFP devices exhibit better seismic performance with respect to classical DCFP bearings with same size, especially, if the superstructure is designed to behave essentially elastic when the lateral capacity of the isolation level is not reached, or the hardening post-yield stiffness of the superstructure is relatively high. Reductions up to 20% in the exceeding probabilities within 50 years related to the ductility demand are achievable using the suggested LIR-DCFP isolator.

Keywords: LIR-DCFP isolator; internal lateral impact; high-friction interface; internal gap; seismic reliability; ductility demand.

1. Introduction

Seismic isolation represents a very effective technique for protecting buildings and infrastructures. The most used devices to achieve seismic isolation are the elastomeric [1] and Friction Pendulum System (FPS) [2] bearings. Frictional isolators typically consist of one or more sliding concave plates with single or multiple inner sliders, depending on the specific configuration of the device. These frictional devices have shown excellent seismic behavior under high magnitude ground motions [3–7]. Among frictional isolators, two examples of devices, commonly used with passive adaptive behavior, are the Double Concave Friction Pendulum (DCFP) [6] and Triple Concave Frictional Pendulum (TCFP) bearings [7,8]. In the following comparisons, DCFP bearings are considered.

Under extreme high magnitude earthquakes, excessive deformations in the isolation devices may occur [9–12]. If the structure is seismically isolated using frictional devices, large base displacements could cause an internal impact between the inner slider and the restraining rims of the sliding surfaces. The internal impact has been indicated as one of the most important causes to the failure of DCFP and TCFP bearings [13,14]. Additionally, the internal lateral impact or the impact between the base of a seismically isolated building against moat walls produces a high increment in the ductility demand of the superstructure [15–20]. Recently, a novel device has been suggested to overcome those problems: the Lateral Impact Resilient Double Concave Friction Pendulum (LIR-DCFP) bearing [21]. The advantage of using a LIR-DCFP bearing over a DCFP device with the same size for both the plates and slider is the improved impact lateral behavior. The new device has an enhanced inner slider with an internal gap and is capable of resisting the internal impact and reducing the inter-story drift demand on the superstructure. The inner slider of the novel isolator consists of two bodies: the top slider and the bottom slider. These two pieces are in contact generating a plane high-friction interface. This interface is activated if the internal impact between the inner slider and the restraining rims occurs. An additional large amount of energy is dissipated if the sliding is produced in the high-friction interface. The concept of the high-friction interface is also different from the sliding regime "V" [7,8] of the TCFP bearing. This

[1] Corresponding author.
E-mail address: gaspar.auadalvarez@polito.it / gaauad@uc.cl

regime "V" is characterized by a stiff pendular force and a low friction force, opposed to the impact lateral behavior of the LIR-DCFP bearing that dissipates an additional amount of energy and limits the impact magnitude. Auad and Almazán [21] analyzed the response of one three-dimensional structure isolated with LIR-DCFP devices, subjected to three different ground motions. Further deterministic and probabilistic analyses have to be conducted considering different properties in the isolation system and superstructure.

Seismic reliability-based design (SRBD) analyses of equivalent two-degrees-of-freedom (dof) models of isolated structures equipped with FPS bearings may be found in [22–26]. Several structural and isolation properties were analyzed in these studies, considering the friction coefficient and the earthquake main characteristics as the relevant random variables. The seismic performance of three-dimensional buildings equipped with FPS bearings has been probabilistically evaluated in Castaldo *et al.* [27] and [28]. The effects due to restraining rims in DCFP and TFPC devices in the performance assessment have been investigated by [17,29,30]. Even if displacement restraint mechanisms are added to isolation devices leading in some cases to a worse performance, base-isolated structures may have lower probabilities to develop damage than non-isolated buildings. According to [17,29,30], the last statement is true for superstructures designed using the loads transmitted by the Maximum Considered Earthquake (MCE) or if the design is carried out using the unreduced loads transmitted by the Design Earthquake (DE) [31].

Considering only DCFP bearings, this research aims to assess the seismic performance of systems equipped with LIR-DCFP bearings having different properties and evaluate their benefits within a comparison with classical DCFP isolators having the same size for both the plates and slider. In this way, it is possible to evaluate the effects of rising the dimension of the internal gap characterizing LIR-DFCP bearings. This paper deals with the seismic reliability of inelastic structures equipped with the above-mentioned frictional bearings. The LIR-DCFP and DCFP isolation systems are represented using a numerical formulation based on rigid body dynamics [21,32] capable of considering the internal lateral impact behavior. A random variable was employed to sample the friction coefficient at large sliding velocity as proposed by Mokha *et al*. [3]. A 1dof model was defined to represent the lateral flexibility of the superstructure. The uncertainty in the seismic inputs was considered by selecting ten different sets of natural seismic records able to match conditional spectra [33–36] for increasing return periods at a specific site in California (i.e., Riverside). Incremental dynamic analyses (IDAs) were performed to assess the probabilistic responses related to the superstructure (in terms of ductility [23,25,26]) and the isolation level (in terms of base displacement [23,25,26]) through an extensive parametric study for different superstructures properties and isolation system characteristics. Using the IDAs data, the probabilities exceeding appropriate limit state thresholds were computed to construct the seismic fragility curves [23,25,26]. Through the convolution integral between the fragility curves and the seismic hazard curves related to the Riverside site, the exceeding probabilities referred to a lifetime of 50 years were assessed to derive the seismic reliability curves [23,25,26].

2. Description of the LIR-DCFP bearing behavior

In this section, a brief description of the lateral behavior of the LIR-DCFP bearing is presented. A complete description may be found in [21].

2.1. General force-displacement relationship of the LIR-DCFP bearing

The LIR-DCFP seismic isolator consists of two facing plates with spherical sliding surfaces. The sliding surfaces of both plates have the same radius of curvature R and frictional coefficient μ_d. The main feature of the device is its enhanced inner slider that consists of two bodies: the top slider and bottom slider. These two bodies are in contact generating a plane high-friction interface. In fact, this plane interface is constructed with a higher friction coefficient denoted as μ_s. The contact between the two inner sliders generates an internal gap that allows the relative displacement between the top and bottom sliders, adding supplementary energy dissipation capacity to the isolator. By ensuring a correct design of the isolation system, the high-friction sliding starts only if the impact between the inner sliders and the restraining rim of the plates occurs. The normalized force-displacement relationship of the device is presented in Figure 1. The force is normalized by the vertical load W applied on its top plate. The total (horizontal) displacement of the top sliding plate relative to the ground is normalized by the effective radius of the device: $R_{eff} = 2R - h_s$, being h_s the total height of the inner slider [6]. This normalization with respect to the geometry of the isolator and the vertical load applied to the device leads to a normalized pendular force with unitary normalized stiffness. In addition, five different stages of the lateral behavior of the isolator are also shown: (1) the beginning of the sliding between the inner sliders and plates, (2) the impact between the sliders and restraining rims of the plates, (3) the sliding between the top and bottom slider, (4) the impact between the top slider and restraining rim of the bottom slider, and (5) the returning of the bottom slider to its original position. The total lateral force in global coordinates F that the bearing

transmits to the superstructure is computed as the sum of three forces: the pendular force F_p, the frictional force F_μ and the impact force F_i. This last force is generated if the relative displacement between the sliders exceeds the size of the internal gap. Between stages (1) and (2), the normalized pendular force increases with a constant slope. The pendular force changes due to the variation of the normal vector that defines the direction of the contact between the spherical surfaces of the plates and the spherical surfaces of the top and bottom sliders. This first sliding generates low friction forces. Between stages (2) and (3), high-friction forces are generated since the sliding is produced in the high-friction interface. During these two stages, the pendular force remains constant because the normal vector, that describes the direction of contact, does not change. During the path between stages (3) and (4), the internal impact force, generated inside the enhanced inner slider, is produced, developing a considerable increment in the total force transmitted by the bearing. The other forces tend to remain constant. Finally, between stages (4) and (5), the returning of the bottom slider is produced, generating a unitary normalized pendular stiffness and low friction forces as the sliding is developed between the spherical surfaces. The collapse mechanisms of frictional isolators have been studied by [13,14]. Under extreme seismic inputs, during the impact between the top and bottom (path between stages (3) and (4)), the yielding of the restraining rims may be observed, leading to damage or even the collapse of the isolator. Another collapse mechanism was also identified, produced by large rotations of the inner slider that lead to bearing instability.
In Appendix A, the results of one experimental test of an LIR-DCFP specimen are presented.

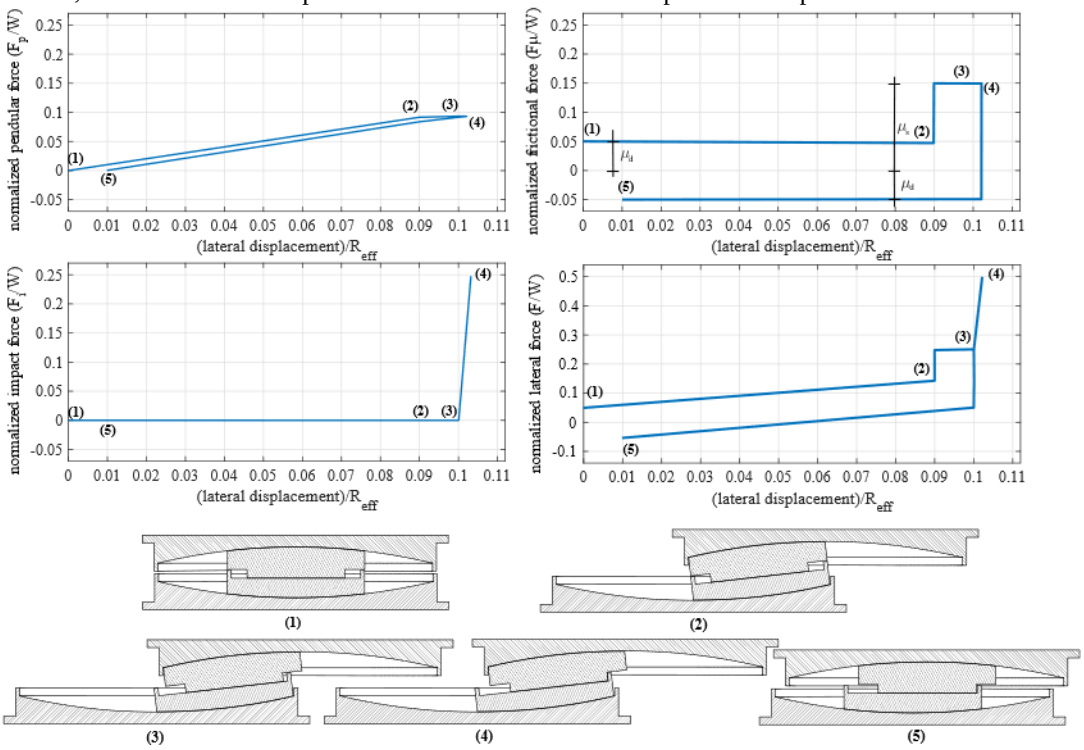

Figure 1: General normalized force-displacement relationship for LIR-DCFP bearings (modified from Auad and Almazán [21]).

2.2. Forces developed inside the isolator

The three-dimensional formulation for modeling frictional isolators, proposed by Bao and Becker [32] and used in the model suggested by Auad and Almazán [21], is based on rigid body dynamics. The numerical models were implemented in the MATLAB environment [37]. It is necessary to define a specific number of sets of contact points to compute the forces that the device transmits to the superstructure. The number of sets of contact points must be equal to the number of contacts between the different bodies that form the device. In detail, four contacts points for each set of contact points have been defined. The same number of contact points has been used in previous studies [21,32]. On the one hand, three sets of four contact points are needed to model the LIR-DCFP bearing because there are three sliding interactions: (i) top plate - top slider, (ii) top slider - bottom slider, and (iii) bottom slider - bottom plate. On the other hand, only two sets are required to model the DCFP because there are only two sliding interactions: top plate - inner slider, and (ii) inner slider - bottom plate. The spatial representations of the contact points used to model both frictional isolators are shown in Figure 2. As shown in Figure 2, every contact point has its projection point on another body. For example, the contact point A_1, that is located on the top surface of the inner slider, has its projection point on the spherical sliding surface of the top plate. This projection point is denoted as A_1'.

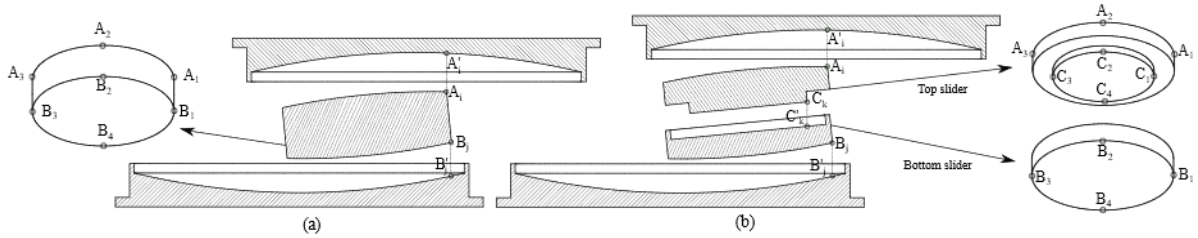

Figure 2: Contact points: (a) DCFP bearing; (b) LIR-DCFP bearing (modified from Auad and Almazán [21]).

By tracking the position $\boldsymbol{r}$ and velocity $\dot{\boldsymbol{r}}$ of each contact point, it is possible to determine the magnitude of the normal force N, the friction force $\boldsymbol{f_\mu}$, and the impact force $\boldsymbol{f_{imp}}$ acting on each couple contact - projection points [21]. For example, the magnitude of the normal force N_{A_1} and friction force $\boldsymbol{f_{\mu,A_1}}$ generated between points A_1 and A_1' can be computed using the following expressions:

$$N_{A_1} = \begin{Bmatrix} k_{A_1}\left(\boldsymbol{r_{A_1}}(3) - \boldsymbol{r'_{A_1}}(3)\right) + c_{A_1}\left(\dot{\boldsymbol{r}}_{\boldsymbol{A_1}}(3) - \dot{\boldsymbol{r}}'_{\boldsymbol{A_1}}(3)\right) & , & \text{if}\left(\boldsymbol{r_{A_1}}(3) - \boldsymbol{r'_{A_1}}(3)\right) \geq 0 \\ 0 & , & \text{otherwise} \end{Bmatrix} \quad (1)$$

$$\boldsymbol{f_{\mu,A_1}} = -\mu_d N_{A_1} \boldsymbol{z_{A_1}} \quad (2)$$

in which k_{A_1} and c_{A_1} are the stiffness and damping coefficient of the interaction between the two points, $\boldsymbol{r_{A_1}}(3)$ and $\boldsymbol{r'_{A_1}}(3)$ are the third component of the vector that describes the position of points A_1 and A_1', $\dot{\boldsymbol{r}}_{\boldsymbol{A_1}}(3)$ and $\dot{\boldsymbol{r}}'_{\boldsymbol{A_1}}(3)$ are the third component of the vector that describes the velocity of points A_1 and A_1', μ_d is the friction coefficient, and the vector $\boldsymbol{z_{A_i}} = \left[z_{A_{1,x}}, z_{A_{1,y}}\right]^T$ contains the dimensionless hysteretic parameters of the biaxial Bouc-Wen's model [38]. These dimensionless parameters allow to model the friction phenomenon. While the norm of $\boldsymbol{z_{A_i}}$ is equal to one during the sliding phase, values less than one imply sticking phase. The contact force between points A_1 and A_1' can be arranged in a three-dimensional vector in local coordinates as follows:

$$\boldsymbol{f_{cont,A_1}} = [\boldsymbol{f_{\mu,A_1}};\ N_{A_1}] \quad (3)$$

The contact forces must be rotated to the global coordinate system and then projected to the global degrees-of-freedom to obtain, for example, the lateral force in global coordinates transmitted by the isolator to the superstructure described in Section 2.1. In this paper, with the purpose to compute the friction force $\boldsymbol{f_\mu}$ developed between contact and projection points located in spherical surfaces, the nonlinear dependence of the friction coefficient μ_d with the sliding velocity $\dot{v}$ is considered using the expression provided by Mokha *et al.* [3] as follows:

$$\mu_d = \mu_{max} - (\mu_{max} - \mu_{min})\exp(-\alpha\dot{v}) \quad (4)$$

in which, μ_{max} is the friction coefficient at high sliding velocity, μ_{min} is the friction coefficient at very slow sliding velocity and α is the rate parameter. In this study, the rate parameter has been set equal to 30 sec/m and the ratio between μ_{max} and μ_{min} has been set equal to 2. The friction forces generated in the high-friction interface are computed assuming a constant friction coefficient μ_s. This high-friction coefficient is assumed to be equal to $2\mu_{max}$.

3. Equivalent dynamic models for base-isolated structures with DCFP and LIR-DCFP devices

In this study, simplified two-dimensional models are developed to analyze the dynamics response of seismically isolated structures. As the aim of this research is to assess the benefits of using LIR-DCFP bearings, two types of seismic isolators are considered to perform a comparison between DCFP and LIR-DCFP bearings. The isolation system is represented by one two-dimensional isolator using the approaches based on rigid body dynamics [21,32], considering three sets of two contact points for LIR-DCFP bearings and two sets of two contact points for DCFP isolators because the two contact points out of plane are not activated for each set. The superstructure is modelled by a 1dof system that exhibits nonlinear behavior in the lateral direction. The two simplified models are shown in Figure 3. The model of the LIR-DCFP bearing has 5dof because this device has one additional rigid body with two additional dof (i.e., one translational and one rotational) with respect to the DCFP device. The rotation of the top plate of both

isolators is considered constrained. The rotations of the inner sliders can be considered dof to account, for example, the angle at which the frictional force is transmitted. In Figure 3, the dynamic parameters of the superstructure have been signaled, being: m_s and m_b the masses of the superstructure and the base, respectively; k_s the linear initial stiffness in the lateral direction; c_s the damping coefficient in the lateral direction (a critical damping ratio of $\xi_s = 0.02$ has been used); and, u_y is the lateral yielding displacement of the superstructure. The mass ratio is defined as $\gamma = m_s/(m_s + m_b)$ [39]. The critical damping ratio for the isolation level is assumed zero. If the lateral period of the superstructure T_s is known, it is possible to compute the initial stiffness as $k_s = (2\pi/T_s)^2 m_s$. In this study, a total mass of $(m_s + m_b) = 500$ kN × sec^2/m was used. By setting the mass ratio γ, the superstructure mass can be computed as $m_s = \gamma(m_s + m_b)$.

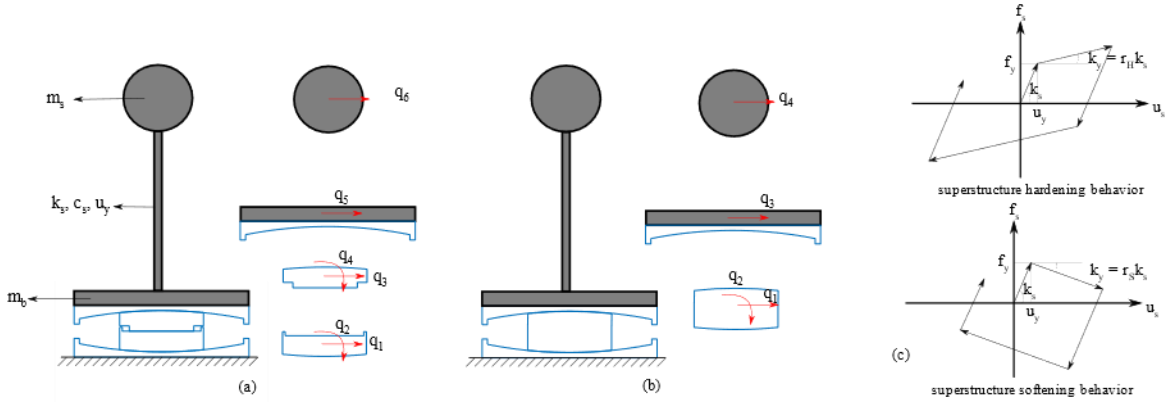

Figure 3: Simplified model of an inelastic building isolated with frictional devices: (a) Isolation system composed of LIR-DCFP bearings; (b) Isolation system composed of DCFP bearings; (c) Superstructure behavior. The term q denotes the dof considered.

The nonlinear lateral force of the superstructure is modeled using a Bouc-Wen element [40], as follows:

$$f_s = r_{H|S} k_s u_s + (1 - r_{H|S}) f_y z_s \tag{5}$$

in which, $f_y = k_s u_y$ is the yield force, $r_{H|S}$ is the stiffness ratio (the subscript depends on the post-yield behavior, being r_H for hardening behavior or r_S for softening behavior (Figure 3(c))), u_s is the displacement of the superstructure, $\dot{u}_s$ is the rate of lateral displacement and z_s is the hysteretic parameter of the superstructure [38]. Note that, the post-yield stiffness can be computed as $k_y = r_{H|S} k_s$. The hysteretic parameter z_s allows to model the nonlinear behavior of the element. If the absolute value of z_s is less than one, the lateral behavior is represented by the initial stiffness k_s; if the absolute value of z_s is equal to one, the behavior is characterized by the post-yield stiffness.

Solving the differential equations of motion [41] through the ode23t solver available in the MATLAB environment [37], the time-history responses of a structure isolated by DCPF and LIR-DCFP bearings subjected to the H-E05140 component of the El Centro Array #4 record (Imperial Valley-06 earthquake, 2010) [42] have been evaluated. The results are shown in Figure 4 in terms of both u_s and (horizontal) base displacement u_b (including the internal gap displacement for the LIR-DCFP device) to highlight the importance to analyze the impact as well as the advantages deriving from the LIR-DCFP bearings. The following parameters [22–26] were used: superstructure period along lateral direction T_s equal to 0.6 sec, $\gamma = 0.7$, superstructure yielding lateral displacement u_y equal to 2 cm (superstructure yield base shear coefficient equal to 0.1565), $R_{eff} = 2.25$ m (isolated period: $T_b = 2\pi\sqrt{R_{eff}/g} =$ 3 sec), $\mu_{max} = 0.07$, $\mu_{min} = 0.035$, $\mu_s = 0.14$, and r_H=0.05. For the both isolators, DCFP and LIR-DCFP bearings, the lateral capacity is defined as the lateral horizontal displacement of the top plate with respect to the bottom plate (or the ground) needed to observe the impact between the inner slider and the restraining rims of the spherical sliding surfaces. For the LIR-DCFP bearing, a lateral capacity of 25 cm was considered with an internal gap of 5 cm. Whereas, two lateral capacities were considered for the DCFP bearings. The first DCFP device has sliding plates of the same size adopted for the LIR-DCFP bearing (i.e., a lateral capacity of 25 cm). The second considered DCFP isolator has a lateral capacity of 30 cm. In Figure 5, an example of the geometry of the three isolators is shown: the dimensions of the plates are slightly bigger to allow the lateral capacity due to the rotation of the slider. The results show that the maximum displacement of the superstructure $u_{s,max}$ is reduced from 12 cm to 7.7 cm by using the LIR-DCFP bearings, decreasing the ductility demand $\mu = u_{s,max}/u_y$ from 6 to 3.85. The demanded ductility of the superstructure equipped with LIR-DCFP bearing is lower than the ductility demanded in the building isolated through a larger capacity DCFP device due to the infinite curvature of the internal gap combined with a higher friction coefficient. As shown in the

work carried out by Bao and Becker concerning the inelastic response of base-isolated subjected to extreme seismic loads [15], if the internal impact is observed, the forces generated in the isolation system tend to have higher magnitudes than the forces developed in the superstructure. Note that the impact triggers the nonlinear behavior of the superstructure. Since the inelastic range of the superstructure is characterized by low stiffness, it is not possible to compensate the transient load of the impact with the inelastic internal force developed in the superstructure. As a result of the described phenomenon, an important rise in the inertial forces is developed in the building [19,20].

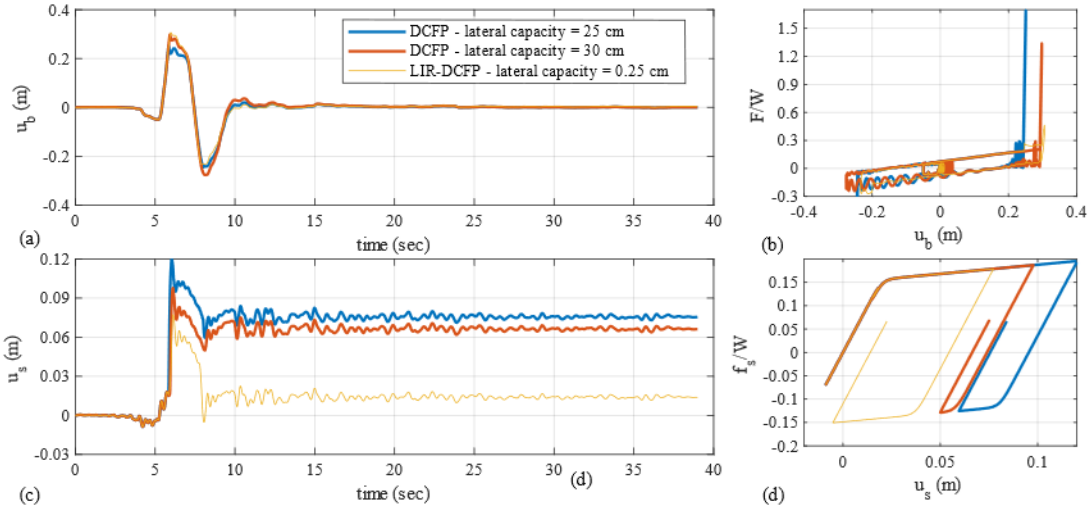

Figure 4: Comparative dynamic response of an isolated structure with DCFP bearings or LIR-DCFP bearings: (a) Base displacement; (b) Hysteretic loops of the isolation system; (c) Superstructure displacement; (d) Hysteretic loops of the superstructure.

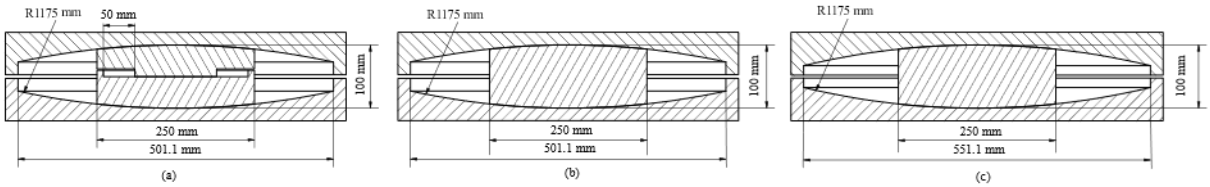

Figure 5: Geometry of the compared isolators (a) LIR-DCFP bearing with a lateral capacity of 25 cm and an internal gap of 5 cm; (b) DCFP bearing with a lateral capacity of 25 cm; (c) DCFP bearing with a lateral capacity of 30 cm.

4. Uncertainties within the seismic reliability assessment

The friction coefficient and earthquake event characteristics have been selected as the relevant random variables. Other aleatory uncertainties corresponding to the mechanical and geometrical properties of the superstructure and the isolation device are not considered as random variables since they do not produce great effects on the statistical values of the response parameters, especially for high values of the isolation degree $I_d = T_b/T_s$ [43–45]. In these cases, the response is mainly governed by the frictional isolators with their most relevant uncertainty: the friction coefficient.

Experimental data on the frictional isolators, described in Mokha *et al.* [3] and Constantinou *et al.* [4], show the variability of the frictional phenomenon depending on some factors. Referring to the two curved surfaces of the LIR-DCFP bearing, the aleatory uncertainty on the sliding friction coefficient at large velocity (i.e., μ_{max}) has been modelled adopting an appropriate Gaussian probability density function (PDF), truncated on both sides to 3% and 7% with a mean value equal to 5% and a coefficient of variation equal to 0.17, as presented in [25,26,46]. From this Gaussian PDF, 15 values were sampled using the Latin Hypercube Sampling (LHS) method [47,48]. The friction coefficient of the high-friction interface of the LIR-DCFP bearing μ_s has been assumed to be correlated with the maximum value of μ_d (i.e., $\mu_s = 2\mu_{max}$).

An intensity measure (IM) is introduced into the reliability analysis to consider the uncertainties of the seismic input intensity, whereas the uncertainties on the characteristics of the records are taken into account by means of a set of natural ground motions. In this work, the selected IM is the spectral acceleration at the isolated period $S_a(T_b)$. Two isolated periods were considered $T_b = 3$ and $T_b = 5$ sec. The parameter $S_a(T_b)$ is associated with a particular location and soil condition and linked with a specific return period T_r according to the seismic hazard of the specific site. Ten different return periods were selected (43; 144; 289; 475; 949; 1,485; 2,475; 3,899; 7,462; and 10,000 years) to

determine ten corresponding values for the IM (i.e., 0.02g, 0.05g, 0.09g, 0.12g, 0.17g, 0.21g, 0.26g, 0.32g, 0.40g and 0.44g for $T_b = 3$ sec; 0.01g, 0.02g, 0.05g, 0.07g, 0.11g, 0.14g, 0.18g, 0.21g, 0.27g and 0.29g for $T_b = 5$ sec; being g the gravity acceleration). The algorithm proposed by Baker and Lee [34] was employed to perform the ground motion selection. In the following subsection, the details of the procedure are presented.

4.1. Ground motion selection matching the Conditional Spectrum

Assuming that the analyzed dynamic systems are located in Riverside, California (latitude/longitude = 33.979/-117.335) with a class C soil ($V_s = 537$ m/sec), it is possible to determine the magnitude M and the distance R of the mean causal earthquake related to a specific return period. These parameters were obtained from de-aggregation of the ground motion hazard using the Unified Hazard Tool [49]. Additionally, it is also possible to determine the value of the IM $= S_a(T_b)$) linked to each return period T_r. The de-aggregation information allows determining a Conditional Mean Spectrum (CMS) [50] for each considered return period. The used conditional periods are equal to the two considered isolated periods: $T^* = T_b = 3$ sec and $T^* = T_b = 5$ sec. The models of Boore *et al.* [51] and of Baker and Jayaram [52] were employed to construct the CMSs (Figure 6).

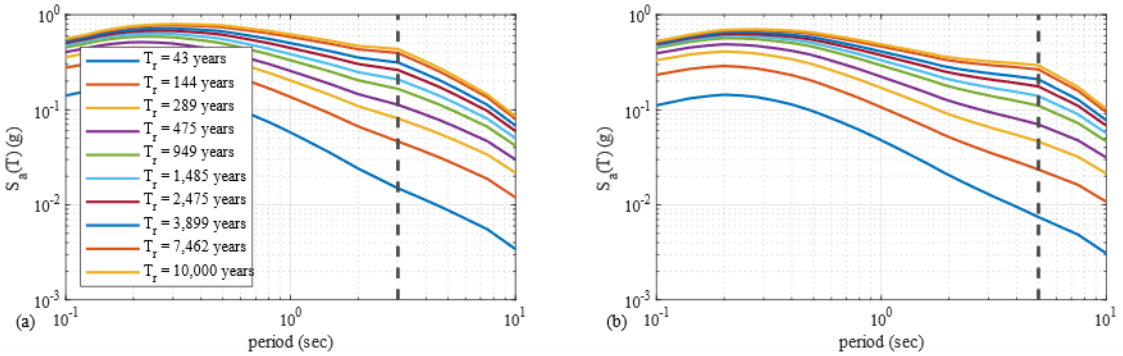

Figure 6: Conditional Mean Spectra for different conditioning period: (a) $T^* = 3$ sec; (b) $T^* = 5$ sec.

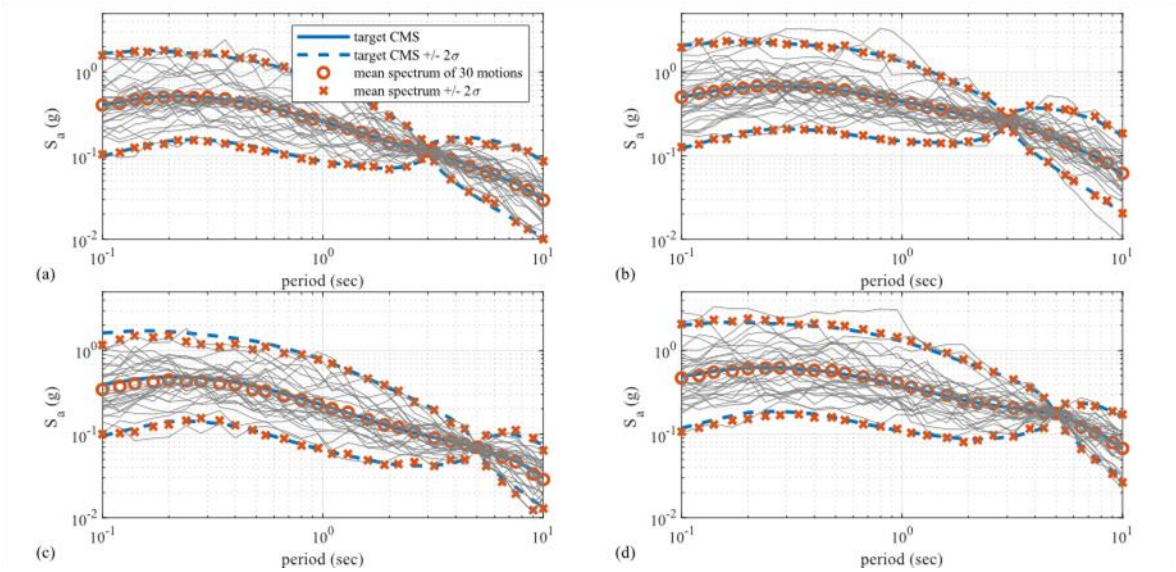

Figure 7: Spectra of the scaled selected ground motions for different T_r and conditioning periods T^*: (a) $T_r = 475$ years and $T^* = 3$ sec; (b) $T_r = 2{,}475$ years and $T^* = 3$ sec; (c) $T_r = 475$ years and $T^* = 5$ sec; (d) $T_r = 2{,}475$ years and $T^* = 5$ sec.

The ground motion selection was performed matching the Conditional Spectra (CSs) [33,35] and considering their distribution for each hazard level (i.e., return period T_r). The distribution of the target spectrum is contemplated by including the conditional standard deviation. For each couple of return period - isolated period, a set of 30 seismic records was selected. In this way, for each considered isolated period T_b, ten different sets of 30 ground motions scaled at the different IM $= S_a(T_b)$ values, were chosen (see Appendix B). All the selected natural seismic records were modified only by scaling the amplitude to match the IM value [23,25,26]. The spectra of four sets of 30 seismic records linked to $T_r = 475$ and $T_r = 2{,}475$ years for isolated periods of $T_b = 3$ and $T_b = 5$ sec are shown in Figure 7.

5. Design of the isolation system and superstructure

The design of the isolation system and superstructure were carried out by the criteria of the ASCE/SEI 7-16 standard [31]. The two-dimensional model of the superstructure equipped with DCFP bearings presented in Section 3 was employed to design both the isolation system lateral capacity and the superstructure properties. Since the main objectives of this research are to assess a comparative seismic performance analysis between LIR-DCFP devices and classical DCFP isolators with the same size and to evaluate the effects of rising the internal gap of LIR-DCFP bearings, the design of the base-isolated structures is the same for the both types of bearings.

The maximum (horizontal) base displacement D_M was estimated using the Response History Analysis (RHA) procedure. A total of 30 seismic records related to $T_r = 2{,}475$, for each considered isolated period, scaled to the same ordinate in terms of spectral acceleration of the Maximum Considered Earthquake (MCE) spectrum were used to estimate the maximum base displacement achieving a more effective design as remarked in [23,26,46]. The MCE level corresponds to an earthquake with a return period of 2,475 years. The spectra of the scaled selected ground motions linked to $T_b = 3$ sec and $T_b = 5$ sec are those presented in Figure 7((b) and (d)), respectively. The lower bound of the friction coefficient at large velocity $\mu_{max} = 0.03$, characterizing the PDF (Section 4), was employed to design the lateral capacity of the isolation system. The lateral capacity was defined using the mean value of the maximum base displacement responses. The American code requires an increment of the maximum displacement capacity to account for accidental torsion that shall not be taken less than 1.15 times the D_M. This minimum limit was employed in this study, defining the total lateral capacity as $D_{TM} = 1.15D_M$. The lateral capacities of both considered isolation systems for $T_b = 3$ sec and $T_b = 5$ sec are reported in Table 1. In this way, the two isolators have the same size for both the plates and slider. As for the LIR-DCFP device, the dimension of the internal gap has to be added as developed in the parametric analysis described in the next sections.

The yielding lateral displacement of the superstructure, defined as $u_y = f_y/k_s$ (Figure 3), is computed using the unreduced lateral seismic design force on elements above the base level V_{st} (i.e., $f_y = V_{st}$), employing the Equivalent Lateral Force (ELF) procedure with the upper bound value of the friction coefficient at large velocity of sliding: $\mu_{max} = 0.07$.

Combining the RHA and ELF procedures, the isolation lateral capacities are larger and the superstructures present overstrength resistances, being designed to behave elastic if the internal impact is not observed. Several researchers have studied the effects of allowing the inelastic response of simplified models, concluding that the yielding of isolated buildings generates significantly greater ductility demands than in a conventional fixed-base structure [53,54]. In the following parametric analysis, the numerical coefficient related to the type of force-resisting system above the isolation system R_I (reduction factor) [31] will be applied, allowing inelastic behavior of the superstructure before reaching the lateral capacity of the isolation system with respect to the different seismic inputs [55]. In cases where the parameter R_I is greater than one, the reduced design lateral seismic force is computed as V_{st}/R_I. With this magnitude of the design force, the superstructure has to be designed and the corresponding yielding displacement applies:

$$u_y = \frac{V_{st}}{k_s R_I} = \frac{u_y^{(R_I=1)}}{R_I} \tag{6}$$

in which, $u_y^{(R_I=1)} = V_{st}/k_s$ is the yielding displacement computed without reducing the lateral seismic design force. Table 1 reports the values of $u_y^{(R_I=1)}$ for the different structural properties adopted in this study.

Table 1: Design parameters of base-isolated systems

Isolation period, T_b (sec)	Superstructure period, T_s (sec)	Lateral capacity of the bearing (cm)	$u_y^{(R_I=1)}$ related to cases with γ = 0.7 (cm)	$u_y^{(R_I=1)}$ related to cases with γ = 0.9 (cm)
3	0.3	41	0.46	0.53
	0.6	41	1.86	2.13
	0.9	41	4.18	4.79
5	0.3	54	0.31	0.34
	0.6	54	1.27	1.37
	0.9	54	2.84	3.06

6. Parametric study within incremental dynamic analysis (IDA)

Performing incremental dynamic analyses (IDAs) is the first step to determine the seismic reliability of non-linear base-isolated equivalent systems equipped with DCFP and LIR-DCFP bearings. Developing IDAs allows to evaluate the structural responses with respect to increasing IM levels, selected in compliance with the seismic hazard curve of the reference site, as described in Section 4. In the present work, several values related to elastic and inelastic properties of the superstructure, combined with the 15 sampled input values of the friction coefficient at large velocity, are used to estimate the probabilistic distribution of the Engineering Demand Parameters (EDPs) of interest. Within the parametric analysis, the isolated period is taken as $T_b = 3$ sec and $T_b = 5$ sec and the superstructure period as $T_s =$ 0.3, 0.6 and 0.9 sec; the mass ratio is assumed as $\gamma = 0.7$ and $\gamma = 0.9$; the numerical coefficient related to the type of seismic force-resisting system above the isolation system is set as $R_I = 1, 1.25, 1.5$ and 2; the post-yield hardening or softening ratio are taken equal to $r_{H|S} = \pm 0.05$ and $r_{H|S} = \pm 0.1$; furthermore, for the cases of structures equipped with LIR-DCFP bearings, internal gaps ranging from 2 cm to 10 cm with a step of 2 cm have been used. All the combinations of the deterministic parameters lead to a total of 1,152 simplified and equivalent systems. The hardening or softening post-yield behavior is introduced to consider structural cases in which the superstructure is not sensitive or is sensitive to $P - \Delta$ effects. Note that the softening superstructure fails when the strength is completely nullified (Figure 3(c)). Furthermore, it is important to highlight that the instability failure of the isolators was never detected in all simulations.

The differential equations of motion [41] have been repeatedly solved using the ode23t solver available in the MATLAB environment [37]. One IDA of one studied case consists of 4,500 simulations, using 30 seismic records properly selected and scaled to 10 different IM (i.e., $S_a(T_b)$) values (Section 4 and Appendix B), combined with the 15 samples of μ_{max}. The IDAs allow estimating the EDPs. Two EDPs are studied: the maximum (horizontal) displacement of the upper plate of the isolation device relative to the ground $u_{b,max} = |u_b(t)|_{max}$ (this parameter takes into account the total displacement of the isolation devices, summing the sliding in low friction contacts and in the high-friction interface, if any); and the ductility demand of the superstructure $\mu = u_{s,max}/u_y$, where $u_{s,max} = |u_s(t)|_{max}$ is the maximum lateral displacement of the superstructure relative to the base. The response parameters are assumed to follow a lognormal distribution [22–28,46]. This distribution allows estimating the response in terms of different percentile levels. The lognormal distribution is fitted by estimating the sample lognormal mean $mean_{ln}(EDP)$ and the sample lognormal standard deviation $\sigma_{ln}(EDP)$ using the maximum likelihood estimation method and without considering the collapses when the softening behavior is analyzed [22–28,46]. In this way, it is possible to generate the IDA curves illustrated in the next sub-section.

6.1. Incremental dynamic analyses (IDAs) results

The IDAs results regarding the isolation level response $u_{b,max}$ are shown in Figure 8 only for cases with a mass distribution ratio of $\gamma = 07$ and hardening post-yield ratio of $r_H = 0.05$, with an internal gap of 10 cm for the structures equipped with LIR-DCFP bearings, due to space constraints. However, other important results, useful to the reliability assessment, are commented in the text. The maximum lateral displacement of the isolation system is highly influenced by T_b. Both the lognormal mean and dispersion rise by increasing the isolation period (e.g., Figure 8((a), and (e))). In all the analyzed cases, the influence of the parameters T_s, γ and $r_{H|S}$ is slight for low values of R_I but affects the statistics of the maximum displacement demand if the superstructure is designed allowing the nonlinear behavior before the occurrence of the internal impact (i.e., $R_I = 1.25$, $R_I = 1.5$ and $R_I = 2$). For structures characterized by a hardening behavior, a rise in T_s as well as in γ, or a decrease in r_H, leads to a reduction of the $u_{b,max}$ EDP (e.g., Figure 8((e), and (f))). The opposite occurs for softening cases, a rise in T_s as well as in γ, or a decrease in the absolute values of r_S, leads to an increase of the maximum base displacement response. This result is influenced by the increase of the number of collapses monitored for higher absolute values of r_S. For high values of IM (i.e., $S_a(T_b)$) the percentiles of $u_{b,max}$ for structures equipped with LIR-DCFP bearings tends to rise with a higher slope than the cases equipped with DCFP bearings especially for $T_b = 3$ sec (e.g., Figure 8((a), and (c))). This is due to the presence of an additional sliding surface combined with the aleatory uncertainty characterizing the plane high-frictional surface.

The IDAs results regarding the ductility demand μ are plotted in Figure 9. In all the studied cases, the deterministic parameter T_s strongly influences the statistics of this EDP. The lognormal mean decreases if the period of the superstructure rises due to the increase of the yielding displacement (e.g., Figure 9((a), and (b))). For low superstructure period and high values of the parameter R_I (reduction factor), the design yielding displacement is low and can be overpassed more easily leading to higher ductility demand. In all the cases, sensitive or not sensitive to $P - \Delta$ effects, a rise in the mass distribution ratio γ leads to a reduction of the $mean_{ln}(\mu)$. The parameter R_I highly

influences the ductility demand of the superstructure. An increase of this parameter leads to a rise in the EDP because the yielding in the structure is observed for lower values of IM (i.e., $S_a(T_b)$). If the superstructure remains essentially elastic before the impact (i.e., $R_I = 1.0$), the 50th and 84th percentiles decrease if LIR-DCFP bearings are used due to the presence of the internal gap that provides additional energy dissipation and limits the maximum force transmitted to the superstructure if the impact between the inner sliders and the restraining rims of the sliding surfaces is observed (e.g., Figure 9((d), and (h))). Considering superstructures that present hardening behavior, an increase in the post-yield hardening ratio r_H leads to a decrease in the ductility demand. For cases that exhibit softening behavior, an increase of the absolute value of r_S leads to an apparent reduction of the statistics of the ductility demand EDP due to the increase of the number of collapses monitored.

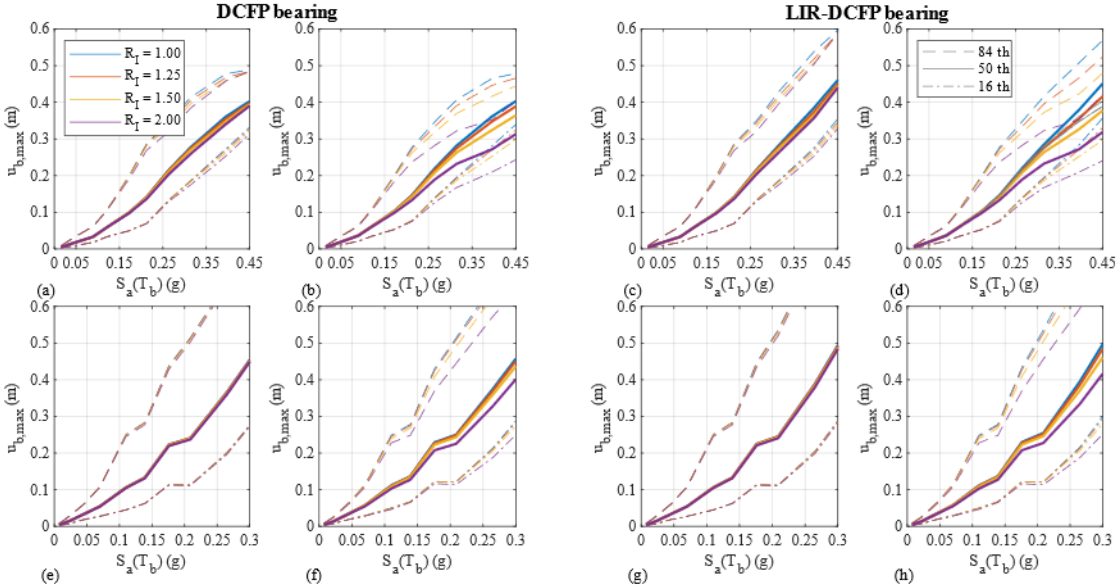

Figure 8: Incremental dynamic analyses curves of the isolation level with $\gamma = 0.7$ and $r_H = 0.05$: (a) DCFP, $T_b = 3$ sec, $T_s = 0.3$ sec; (b) DCFP, $T_b = 3$ sec, $T_s = 0.9$ sec; (c) LIR-DCFP, $T_b = 3$ sec, $T_s = 0.3$ sec; (d) LIR-DCFP, $T_b = 3$ sec, $T_s = 0.9$ sec; (e) DCFP, $T_b = 5$ sec, $T_s = 0.3$ sec; (f) DCFP, $T_b = 5$ sec, $T_s = 0.9$ sec; (g) LIR-DCFP, $T_b = 5$ sec, $T_s = 0.3$ sec; (h) LIR-DCFP, $T_b = 5$ sec, $T_s = 0.9$ sec.

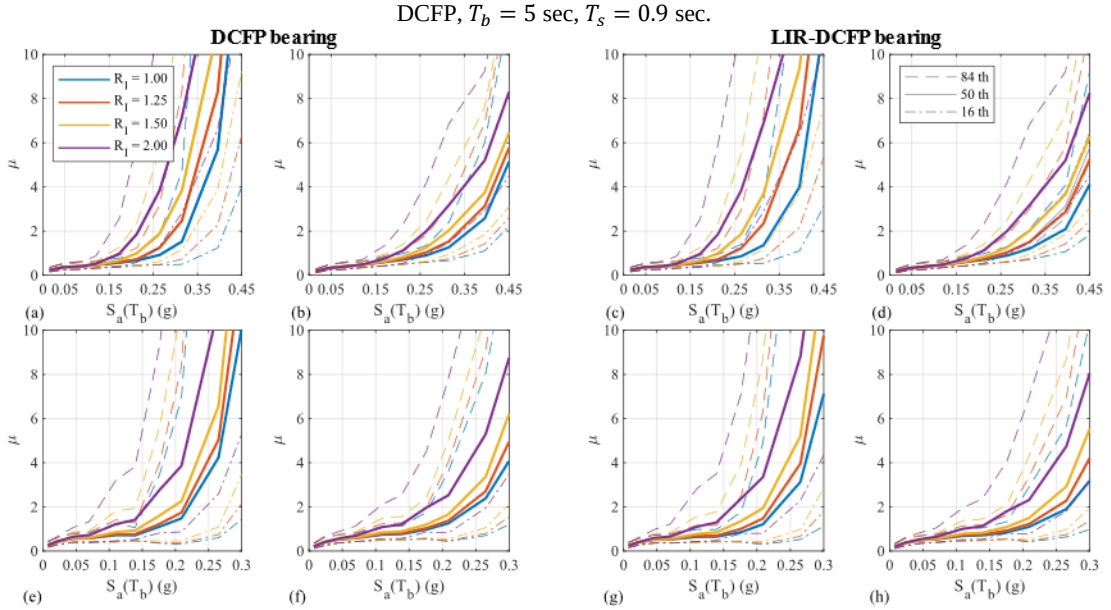

Figure 9: Incremental dynamic analyses curves of the superstructure with $\gamma = 0.7$ and $r_H = 0.05$: (a) DCFP, $T_b = 3$ sec, $T_s = 0.3$ sec; (b) DCFP, $T_b = 3$ sec, $T_s = 0.9$ sec; (c) LIR-DCFP, $T_b = 3$ sec, $T_s = 0.3$ sec; (d) LIR-DCFP, $T_b = 3$ sec, $T_s = 0.9$ sec; (e) DCFP, $T_b = 5$ sec, $T_s = 0.3$ sec; (f) DCFP, $T_b = 5$ sec, $T_s = 0.9$ sec; (g) LIR-DCFP, $T_b = 5$ sec, $T_s = 0.3$ sec; (h) LIR-DCFP, $T_b = 5$ sec, $T_s = 0.9$ sec.

7. Seismic fragility

The next step is the evaluation of the seismic fragility, defined as the probability P_f exceeding a limit state (LS) at each IM level. The LS thresholds need to be defined for the seismic fragility assessment. On the one hand, the performance levels of the isolation system are defined in terms of the maximum (horizontal) displacement of the upper plate of the isolators $u_{b,max}$ (i.e., $\text{LS}_{u_{b,max}} = 5;\ 10;\ 15;\ 20;\ 25;\ 30;\ 35;\ 40;\ 45;\ 50;\ 55$ cm) [23,25,26]. On the other hand, the performance levels related to the superstructure are defined in terms of the ductility demand μ of the superstructure (i.e., $\text{LS}_{\mu} = 1;\ 2;\ 3;\ 4;\ 5;\ 6;\ 7;\ 8;\ 9;\ 10$) [23,25,26]. Although not realistic, several limit state thresholds have been adopted to achieve an accurate numerical assessment of the seismic fragility and, successively, reliability [23,25,26]. The probabilities exceeding the different LSs at each IM level are determined fitting lognormal complementary cumulative distribution function (CCDFs). In cases with softening post-yield behavior (see Figure 3(c)), the fragility evaluation considered the collapse and not-collapse results using the total probability theorem, as carried out in [25,46,56]. In these softening cases, the collapse is reached if the strength of the superstructure is completely nullified.

As an example and due to space constraints, the fragility curves related to the isolation level representing the probability P_f exceeding $\text{LSs}_{u_{b,max}} = 10, 30$ and 45 cm for an isolated period of $T_b = 3$ sec and a hardening post-yield ratio of $r_H = 0.05$ are presented in Figure 10 (for $T_s = 0.3$ sec) and Figure 11 (for $T_s = 0.6$ sec). However, other important results, useful to the reliability assessment, are commented in the text.

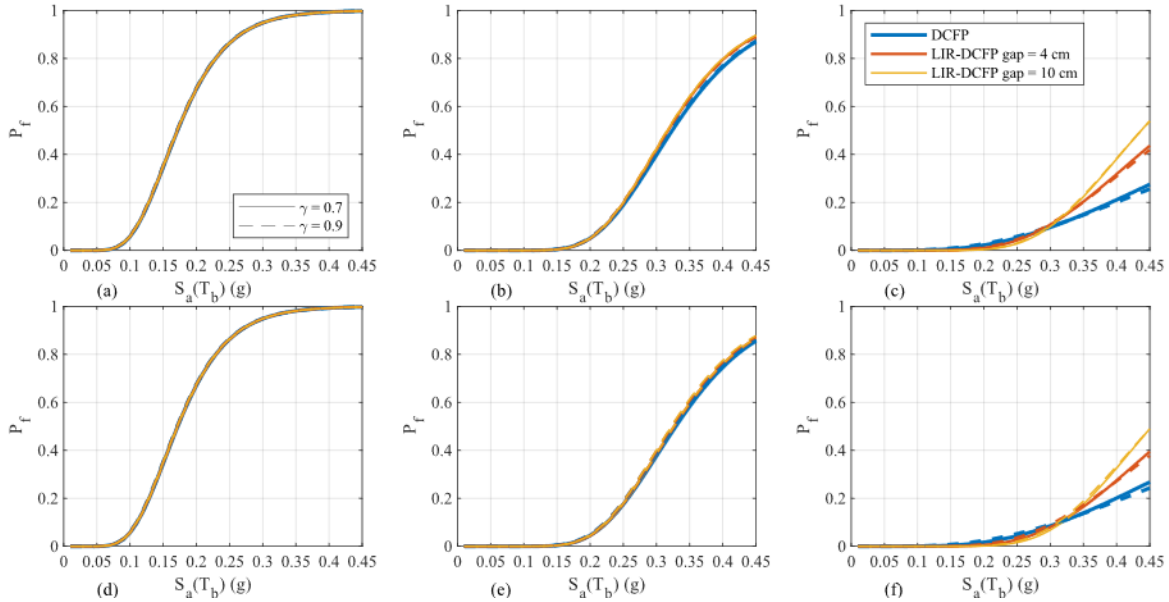

Figure 10: Seismic fragility curves of the isolation level related to $T_s = 0.3$ sec and $r_H = 0.05$: (a) $\text{LS}_{u_{b,max}} = 10$ cm and $R_I = 1$; (b) $\text{LS}_{u_{b,max}} = 30$ cm and $R_I = 1$; (c) $\text{LS}_{u_{b,max}} = 45$ cm and $R_I = 1$; (d) $\text{LS}_{u_{b,max}} = 10$ cm and $R_I = 2$; (e) $\text{LS}_{u_{b,max}} = 30$ cm and $R_I = 2$; (f) $\text{LS}_{u_{b,max}} = 45$ cm and $R_I = 2$.

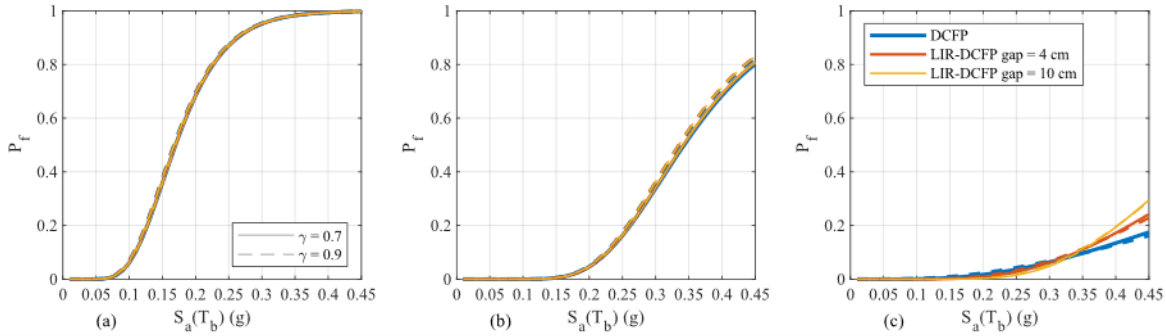

Figure 11: Seismic fragility curves of the isolation level related to $T_s = 0.6$ sec, $r_H = 0.05$ and $R_I = 2$: (a) $\text{LS}_{u_{b,max}} = 10$ cm; (b) $\text{LS}_{u_{b,max}} = 30$ cm; (c) $\text{LS}_{u_{b,max}} = 45$.

The seismic fragility of the isolation level decreases for increasing the LS thresholds. In fact, for low IM and LS thresholds the seismic fragility is higher (e.g., Figure 10(a), and Figure 11(a)). For cases with $R_I = 1$ and $\mathrm{LSs}_{u_{b,max}}$ lower than 40 cm, the fragility curves are slightly affected by the superstructure period T_s and mass ratio γ (e.g., Figure 10(b), and Figure 11(b)). The influence of the superstructure period is stronger for $\mathrm{LS}_{u_{b,max}} = 45$ cm (the internal impact is produced) and $R_I = 2$ (e.g., Figure 10(c), and Figure 11(c)). Under these last conditions, in all the studied cases, an increment in T_s or γ leads to a seismic fragility reduction for the isolation level. The effect of increasing the mass distribution ratio is stronger for the softening behavior. For cases related to superstructures with a hardening lateral behavior, a rise in the parameter r_H leads to a slight increase in the probabilities of exceeding $\mathrm{LS}_{u_{b,max}}$ thresholds. For cases with superstructures sensitive to $P-\Delta$ effects, an increment in the absolute value of r_S leads to a rise in the fragility curves. This increment is due to the higher number of collapses previously monitored. The influence of the internal gap for the LIR-DCFP bearings in the probability exceeding high $\mathrm{LS}_{u_{b,max}}$ thresholds is noticeable. In fact, a rise in the internal gap leads to an increment of the fragility curves due to the additional displacement developed along the high-friction interface (e.g., Figure 10((c) and (f)), and Figure 11(c)).

The fragility curves related to the superstructure for ductility demand thresholds $\mathrm{LS}_\mu = 1, 4$ and 7 are presented in Figure 12 (for $T_s = 0.3$ sec) and Figure 13 (for $T_s = 0.6$ sec). The period of the superstructure T_s influences the fragility curves. The stiffer the structure, the higher probabilities exceeding the LS_μ. In general, higher values of mass ratio γ decrease the fragility curves (e.g., Figure 12(a) and Figure 13(a)).

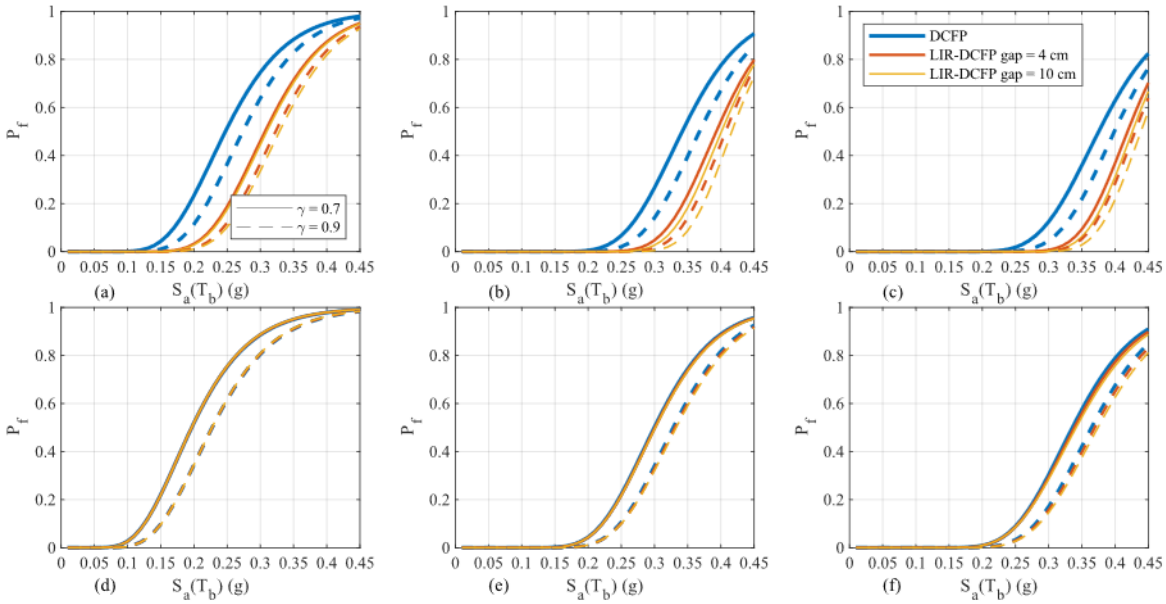

Figure 12: Seismic fragility curves of superstructure related to $T_s = 0.3$ sec and $r_H = 0.05$: (a) $\mathrm{LS}_\mu = 1$ and $R_I = 1$; (b) $\mathrm{LS}_\mu = 4$ and $R_I = 1$; (c) $\mathrm{LS}_\mu = 7$ and $R_I = 1$; (d) $\mathrm{LS}_\mu = 1$ and $R_I = 2$; (e) $\mathrm{LS}_\mu = 4$ and $R_I = 2$; (f) $\mathrm{LS}_\mu = 7$ and $R_I = 2$.

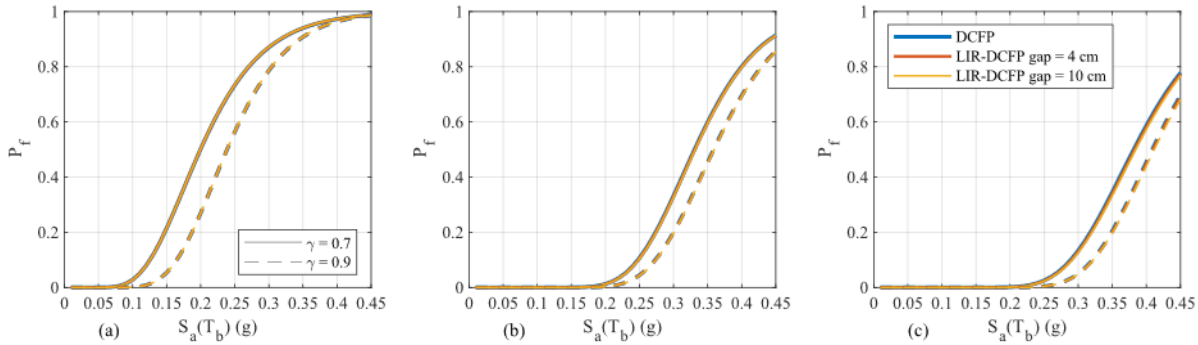

Figure 13: Seismic fragility curves of superstructure related to $T_s = 0.6$ sec, $r_H = 0.05$ and $R_I = 2$: (a) $\mathrm{LS}_\mu = 1$; (b) $\mathrm{LS}_\mu = 4$; (c) $\mathrm{LS}_\mu = 7$.

As expected, an increment in R_I leads to a rise of the probabilities exceeding the LS_μ (e.g., Figure 12((a) and (d))). If the superstructure behaves essentially elastic before the impact (i.e., low values of R_I), an increase of the internal gap reduces the fragility curves demonstrating the advantages of the LIR-DCFP devices, especially for lower T_s (e.g., Figure 12((a), (b), and (c))). This improvement in the seismic performance, in cases that present hardening behavior, increases for higher values of r_H. In cases of superstructures with a softening behavior, the use of the studied seismic isolator is valuable, especially, for structures designed to remain elastic if internal impact is not observed (i.e., $R_I = 1$). These advantages derive from the presence of the internal gap with infinite curvature combined with the higher friction coefficient.

8. Seismic reliability of structures equipped with DCFP and LIR-DCFP bearings

The convolution integral between the defined fragility curves and the seismic hazard curves, expressed in terms of the same IM (i.e., $S_a(T_b)$), allows calculating the mean annual rate exceeding the LSs through the following equation:

$$\lambda_{LS}(EDP > y) = \int_0^\infty P(EDP > y \mid S_a(T_b) = x)|\lambda(\mathrm{d}S_a(T_b) > x)| \tag{7}$$

in which, $\lambda(\mathrm{d}S_a(T_b) > x)$ is the derivative of the hazard curve for $S_a(T_b)$ (i.e., the annual mean rate exceeding the specific value of the IM $= S_a(T_b) = x$) multiplied by an increment of $dS_a(T_b)$; and $P(EDP > y \mid S_a(T_b) = x)$ is the probability of the EDP exceeding y (i.e., a specific LS) given a ground motion with $S_a(T_b) = x$. The term $P(EDP > y \mid S_a(T_b) = x)$ represents the fragility curves computed in Section 7. The evaluation of the seismic reliability of base-isolated systems can be achieved by using a Poisson distribution considering a time frame (e.g., 50 years) on the results of the convolution integral, as follows:

$$P_f(50\text{ years}) = 1 - \exp\left(-\lambda_{LS}(EDP > y) \cdot (50\text{ years})\right) \tag{8}$$

The seismic reliability curves of the isolation level are plotted in logarithmic scale in Figure 14 for $T_b = 3$ sec and $r_H = 0.10$. The increase of R_I leads to a decrease on the probabilities exceeding $LS_{u_{b,max}}$ thresholds. This reduction in the base displacement demand is increased for higher values of T_s (e.g., Figure 14((a), and (c))). This phenomenon decreases the benefits of using LIR-DCFP bearings for the isolation level itself. The main difference in the dynamic behavior of the suggested new frictional isolator is exhibited if the internal lateral impact is observed. A high value of the parameter R_I implies that the yielding of the superstructure is observed before the occurrence of the internal impact. The nonlinear behavior of the superstructure causes an elongation of its fundamental period losing the effectiveness of the seismic isolation technique, expressed in a reduction of the base displacement demand with an increase on the ductility demand of the superstructure (e.g., Figure 14((c), and (f))).

The effects of considering softening post-yield behavior ($r_S = -0.10$) on the maximum base displacement is presented in Figure 15. Under this scenario, the differences in the lateral displacement of the isolation system using DCFP bearings or LIR-DCFP bearings are negligible. The increment in the probabilities exceeding $LS_{u_{b,max}}$ thresholds is generated by an increase in the number of superstructure collapses.

In Figures 16-23, the seismic reliability curves in 50 years of all the studied superstructures are plotted in logarithm scale for the different LS_μ thresholds. Blue lines in the figures represent cases of isolated structures equipped with DCFP bearings. Other colors represent systems equipped with the LIR-DCFP bearings for different gap sizes. In general, the seismic reliability of the superstructure declines for higher values of R_I. The post-yield ratio affects the performance of the studied seismically isolated structures. In fact, an increase of the hardening post-yield ratio r_H leads to a rise in the seismic reliability (hardening behavior: Figures 16, 17, 20 and 21), whereas an increase in the absolute values of r_S (softening behavior: Figures 18, 19, 22 and 23) causes worse seismic performance of the superstructure. The influence of the described parameters of dynamic systems are in concordance with previous studies [23,25,26,46].

The exceeding probabilities are slightly decreased for higher values of γ (e.g., Figure 17((c), and (f))). As mentioned in Section 3, an increment in the inertial forces developed in the superstructure is produced by lateral impacts [19,20]. This rise in the inertial forces increases the ductility demand specially if an important portion of the total mass is concentrated in the base (i.e., lower values of the mass ratio γ). The opposite happens for higher values of γ.

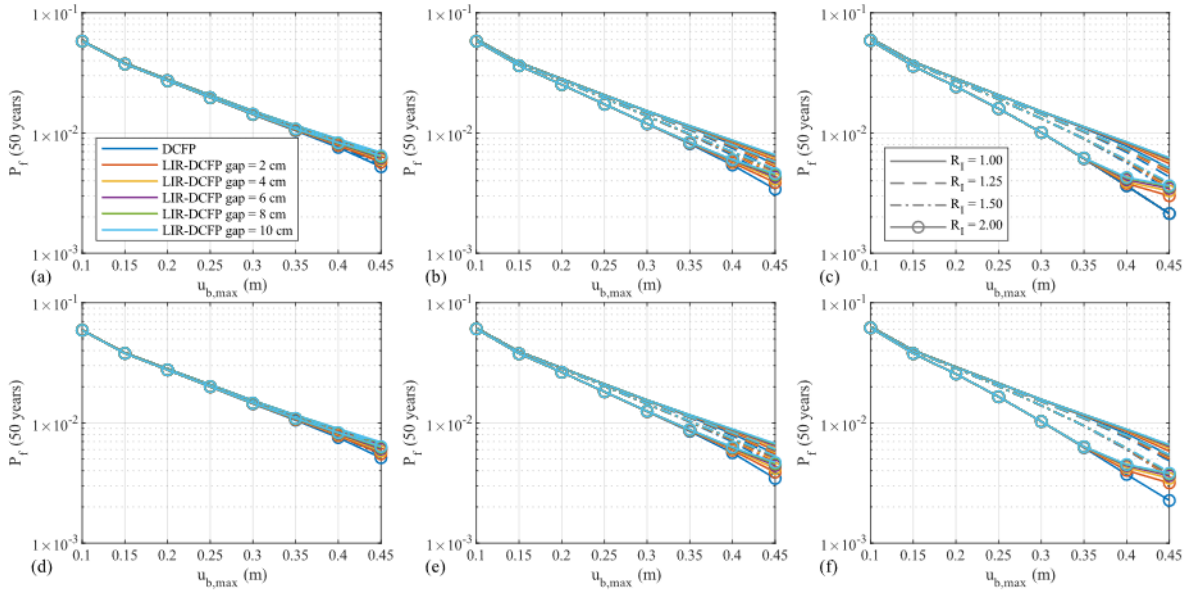

Figure 14: Seismic reliability of the isolation level for $T_b = 3$ sec and $r_H = 0.10$: (a) $\gamma = 0.7$ and $T_s = 0.3$ sec; (b) $\gamma = 0.7$ and $T_s = 0.6$ sec; (c) $\gamma = 0.7$ and $T_s = 0.9$ sec; (d) $\gamma = 0.9$ and $T_s = 0.3$ sec; (e) $\gamma = 0.9$ and $T_s = 0.6$ sec; (f) $\gamma = 0.9$ and $T_s = 0.9$ sec.

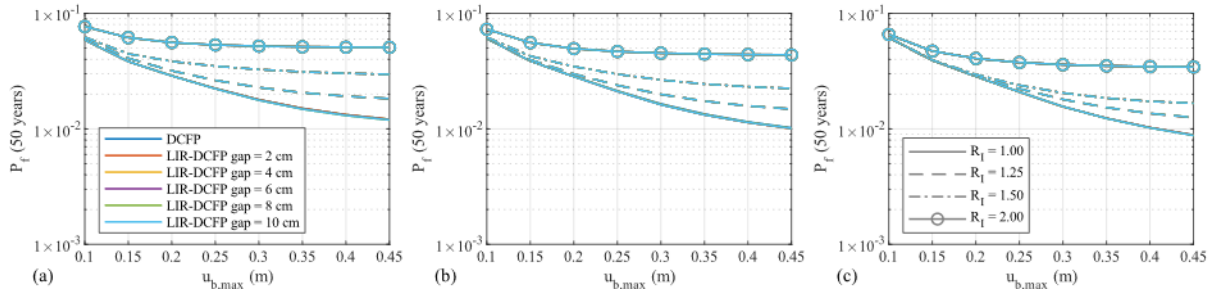

Figure 15: Seismic reliability of the isolation level for $T_b = 3$ sec, $\gamma = 0.7$ and $r_S = -0.10$: (a) $T_s = 0.3$ sec; (b) $T_s = 0.6$ sec; (c) $T_s = 0.9$ sec.

Analyzing the benefits of using the LIR-DCFP bearings, an increase in the internal gap of the enhanced inner slider leads to a better seismic performance of the superstructure (e.g., Figure 16((a), and (d)), Figure 17((a), and (d)), Figure 20((a), and (d)), and Figure 21((a), and (d))). The presence of an internal gap in the inner slider limits the maximum lateral force that the devices can transmit to the superstructure after the internal impact between the inner slider and the restraining rims of the sliding plates, reducing the ductility demand on the isolated building. Furthermore, the high-friction sliding produced by the internal impact dissipates an additional amount of energy. An increase in the size of the internal gap of the LIR-DCFP bearings leads to a larger capacity of frictional energy dissipation, improving the seismic performance. The enhancing of the seismic performance is highlighted, especially, for low values of R_I (e.g., Figure 16((a), and (d)), Figure 17((a), and (d)), Figure 20((a), and (d)), and Figure 21((a), and (d))). It is important to emphasize that in no case the use of LIR-DCFP bearings increases the ductility demand. Consequently, using the suggested isolator ensures quite always a better seismic performance than structures equipped with DCFP isolators having same size for both the plates and slider.

Analyzing cases with hardening post-yield behavior, even for cases with $R_I = 1.25$, $R_I = 1.5$, or $R_I = 2.0$, better seismic performance is achieved using the proposed seismic isolator if the superstructure is stiff and the post-yield hardening ratio is relatively high (e.g., Figure 16((a), and (d)), Figure 17((a), and (d)), Figure 20((a), and (d)), and Figure 21((a), and (d))). On the contrary, for flexible superstructures with lower post-yield hardening ratios, the benefits of using the suggested isolator are slightly lower (e.g., Figure 16(c) and Figure 17(c)).

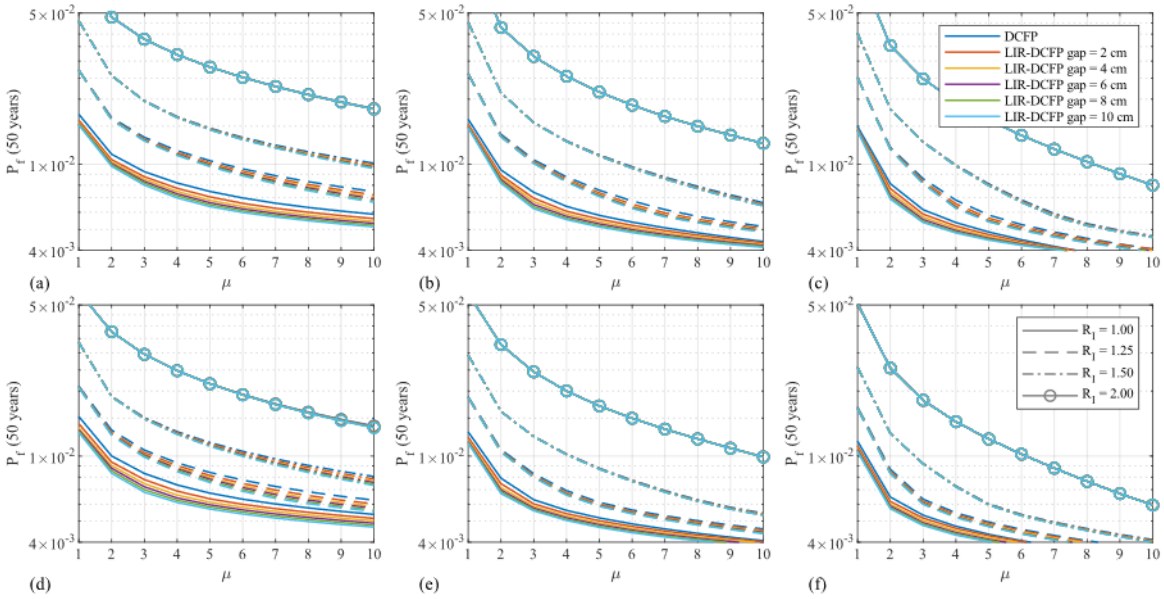

Figure 16: Seismic reliability of the superstructure for $T_b = 3$ sec and $r_H = 0.05$: (a) $\gamma = 0.7$ and $T_s = 0.3$ sec; (b) $\gamma = 0.7$ and $T_s = 0.6$ sec; (c) $\gamma = 0.7$ and $T_s = 0.9$ sec; (d) $\gamma = 0.9$ and $T_s = 0.3$ sec; (e) $\gamma = 0.9$ and $T_s = 0.6$ sec; (f) $\gamma = 0.9$ and $T_s = 0.9$ sec.

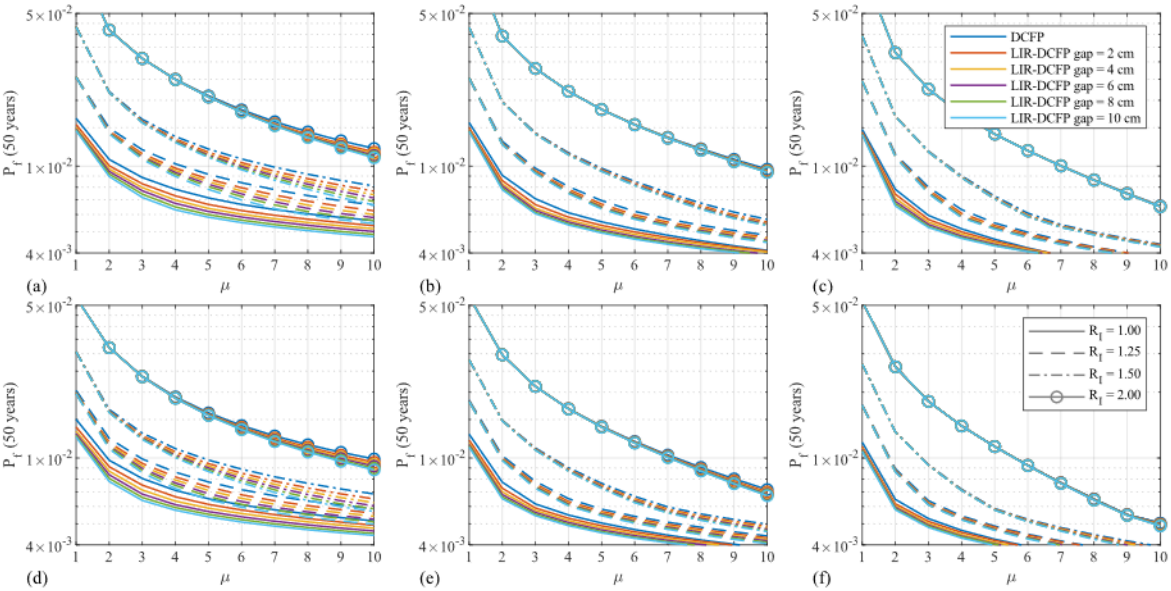

Figure 17: Seismic reliability of the superstructure for $T_b = 3$ sec and $r_H = 0.10$: (a) $\gamma = 0.7$ and $T_s = 0.3$ sec; (b) $\gamma = 0.7$ and $T_s = 0.6$ sec; (c) $\gamma = 0.7$ and $T_s = 0.9$ sec; (d) $\gamma = 0.9$ and $T_s = 0.3$ sec; (e) $\gamma = 0.9$ and $T_s = 0.6$ sec; (f) $\gamma = 0.9$ and $T_s = 0.9$ sec.

For cases with softening post-yield behavior, higher values of the absolute value of r_S strongly affect the ductility demand on the superstructure, decreasing the seismic performance. The benefits of using the proposed frictional device to isolate superstructures sensitive to $P-\Delta$ effects are exhibited for $R_I = 1$ and in some cases with $R_I = 1.25$ (e.g., Figure 18(e), Figure 22, and Figure 23). In all the studied cases with $R_I = 1.5$ or $R_I = 2$, the softening behavior leads to the occurrence of collapse before the occurrence of the internal lateral impact. This phenomenon is observed for post-yield ratios of $r_S = -0.05$ and -0.10. Consequently, the dynamics behavior of systems with these characteristics is the same using DCFP bearings or LIR-DCFP bearings (e.g., Figures 18-19, and Figures 22-23).

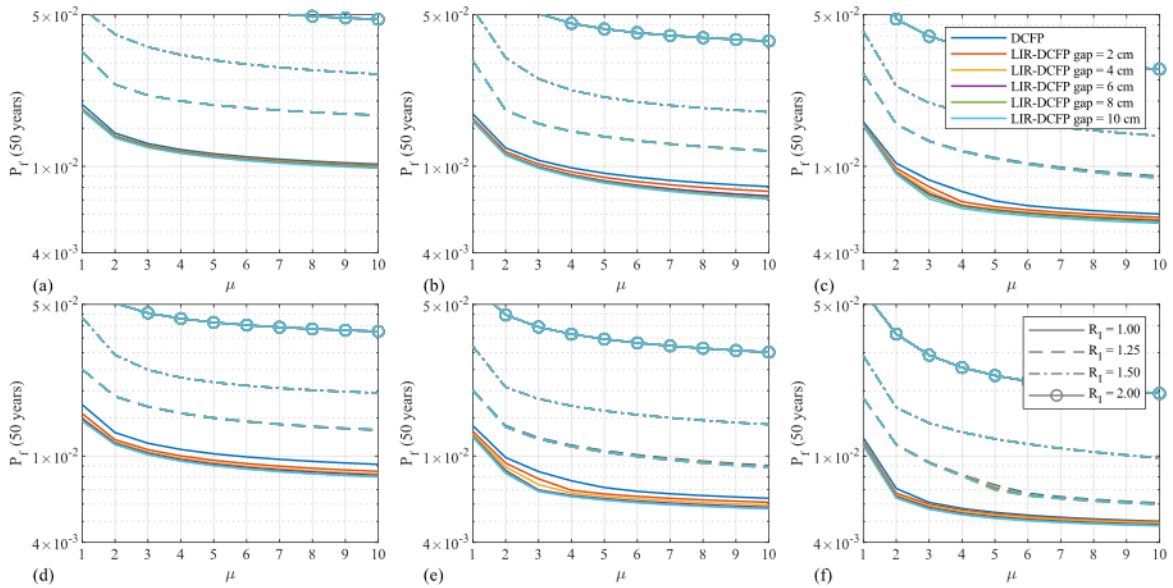

Figure 18: Seismic reliability of the superstructure for $T_b = 3$ sec and $r_S = -0.05$: (a) $\gamma = 0.7$ and $T_s = 0.3$ sec; (b) $\gamma = 0.7$ and $T_s = 0.6\ sec$; (c) $\gamma = 0.7$ and $T_s = 0.9$ sec; (d) $\gamma = 0.9$ and $T_s = 0.3$ sec; (e) $\gamma = 0.9$ and $T_s = 0.6$ sec; (f) $\gamma = 0.9$ and $T_s = 0.9$ sec.

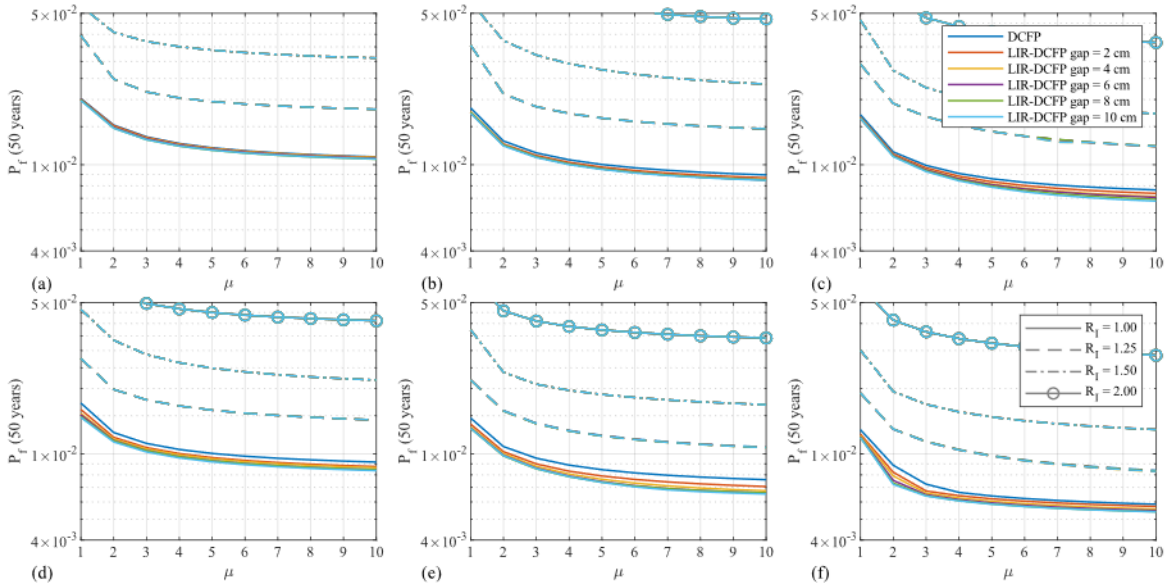

Figure 19: Seismic reliability of the superstructure for $T_b = 3$ sec and $r_S = -0.10$: (a) $\gamma = 0.7$ and $T_s = 0.3$ sec; (b) $\gamma = 0.7$ and $T_s = 0.6$ sec; (c) $\gamma = 0.7$ and $T_s = 0.9$ sec; (d) $\gamma = 0.9$ and $T_s = 0.3$ sec; (e) $\gamma = 0.9$ and $T_s = 0.6$ sec; (f) $\gamma = 0.9$ and $T_s = 0.9$ sec.

These reliability curves (Figures 16-23) can be adopted as SRBD curves according to studies dealing with DCFP devices [25,26] to define relationships between R_I and μ for the superstructure when LIR-DCFP bearings are employed with important design suggestions for the internal gap as well as to assess the performance. Within this last issue, the reduction of the probabilities in 50 years exceeding thresholds of $LS_\mu = 3$ and 5 for cases related to $R_I = 1.00$ and 1.25 having LIR-DCFP bearings instead of DCFP devices is plotted, respectively, in Figures 24 and 25. The results demonstrate an improved seismic performance of buildings equipped with LIR-DCFP bearings. In general, an increment of the size of the internal gap of the inner slider leads to an increase of the reduction of the exceedance probability of the ductility demand thresholds. The increase of the reduction percentage is larger for increasing internal gap values (e.g., Figure 24((a), and (f))). The role of the parameter R_I is crucial to achieve a better seismic performance by using LIR-DCFP bearings. The benefits of using frictional isolators with enhanced inner sliders are increased for low values of R_I (e.g., Figure 24).

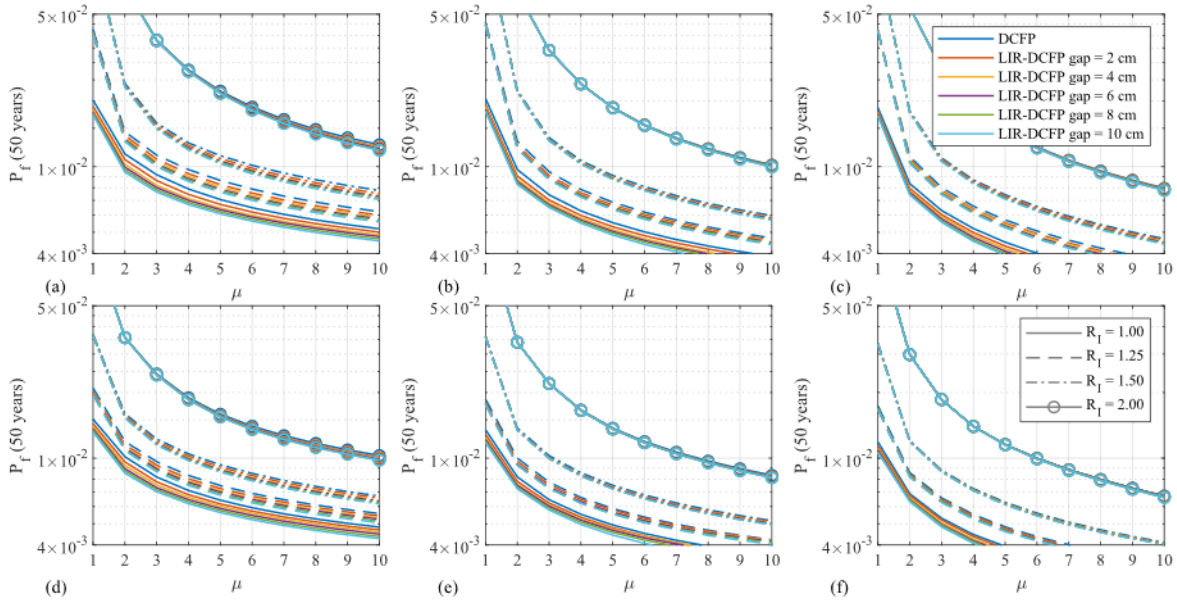

Figure 20: Seismic reliability of the superstructure for $T_b = 5$ sec and $r_H = 0.05$: (a) $\gamma = 0.7$ and $T_s = 0.3$ sec; (b) $\gamma = 0.7$ and $T_s = 0.6$ sec; (c) $\gamma = 0.7$ and $T_s = 0.9$ sec; (d) $\gamma = 0.9$ and $T_s = 0.3$ sec; (e) $\gamma = 0.9$ and $T_s = 0.6$ sec; (f) $\gamma = 0.9$ and $T_s = 0.9$ sec.

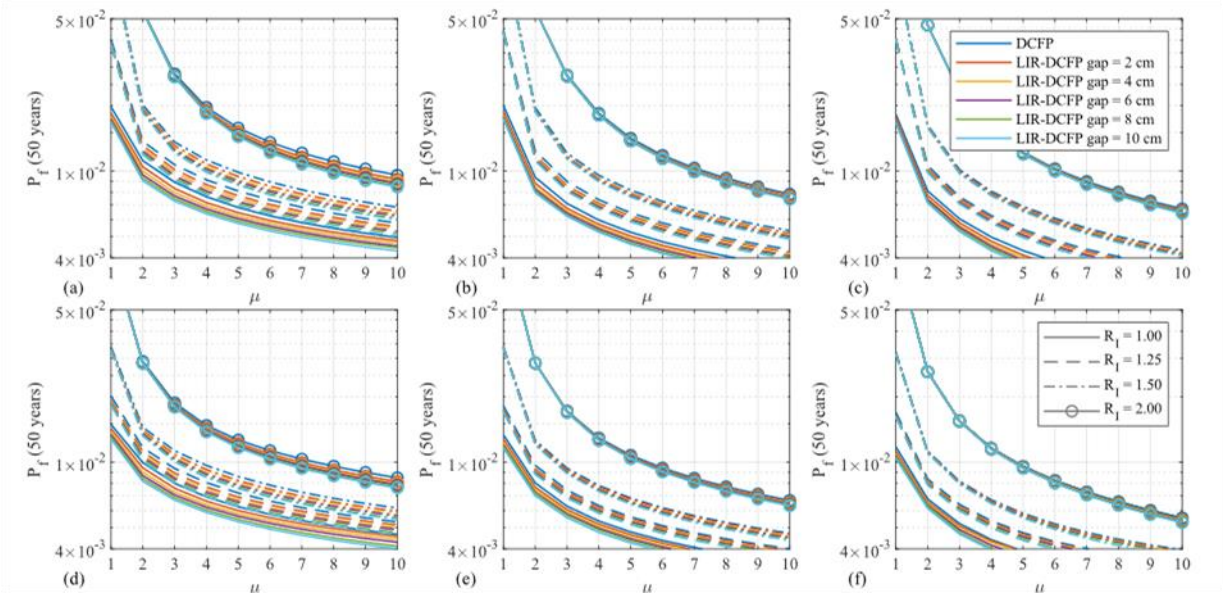

Figure 21: Seismic reliability of the superstructure for $T_b = 5$ sec and $r_H = 0.10$: (a) $\gamma = 0.7$ and $T_s = 0.3$ sec; (b) $\gamma = 0.7$ and $T_s = 0.6$ sec; (c) $\gamma = 0.7$ and $T_s = 0.9$ sec; (d) $\gamma = 0.9$ and $T_s = 0.3$ sec; (e) $\gamma = 0.9$ and $T_s = 0.6$ sec; (f) $\gamma = 0.9$ and $T_s = 0.9$ sec.

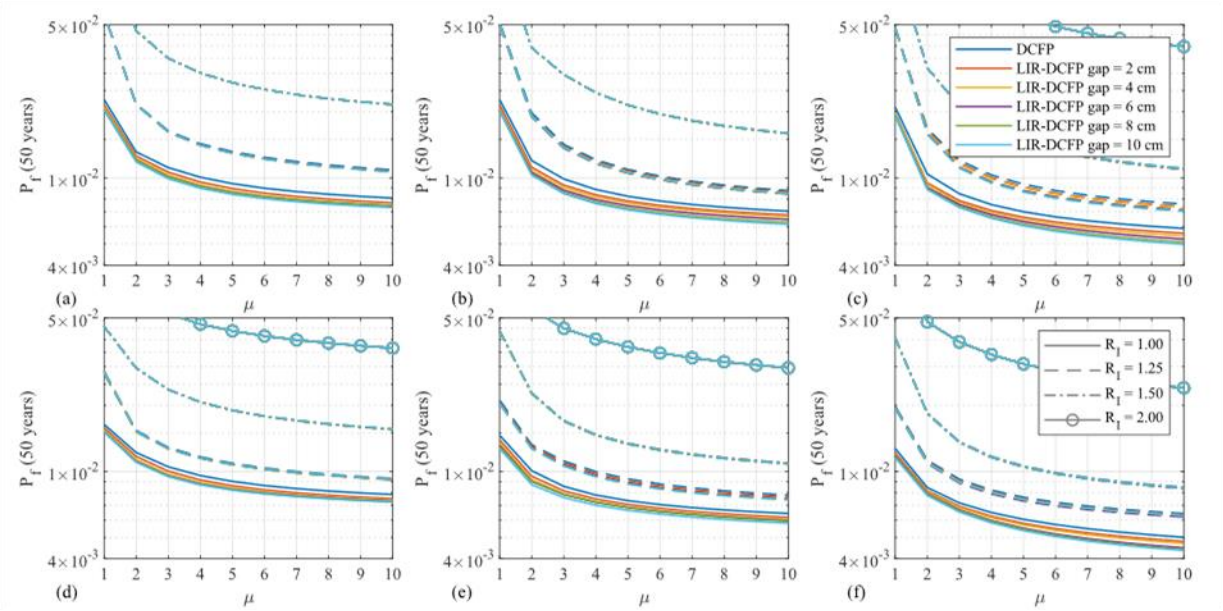

Figure 22: Seismic reliability of the superstructure for $T_b = 5$ sec and $r_S = -0.05$: (a) $\gamma = 0.7$ and $T_s = 0.3$ sec; (b) $\gamma = 0.7$ and $T_s = 0.6$ sec; (c) $\gamma = 0.7$ and $T_s = 0.9$ sec; (d) $\gamma = 0.9$ and $T_s = 0.3$ sec; (e) $\gamma = 0.9$ and $T_s = 0.6$ sec; (f) $\gamma = 0.9$ and $T_s = 0.9$ sec.

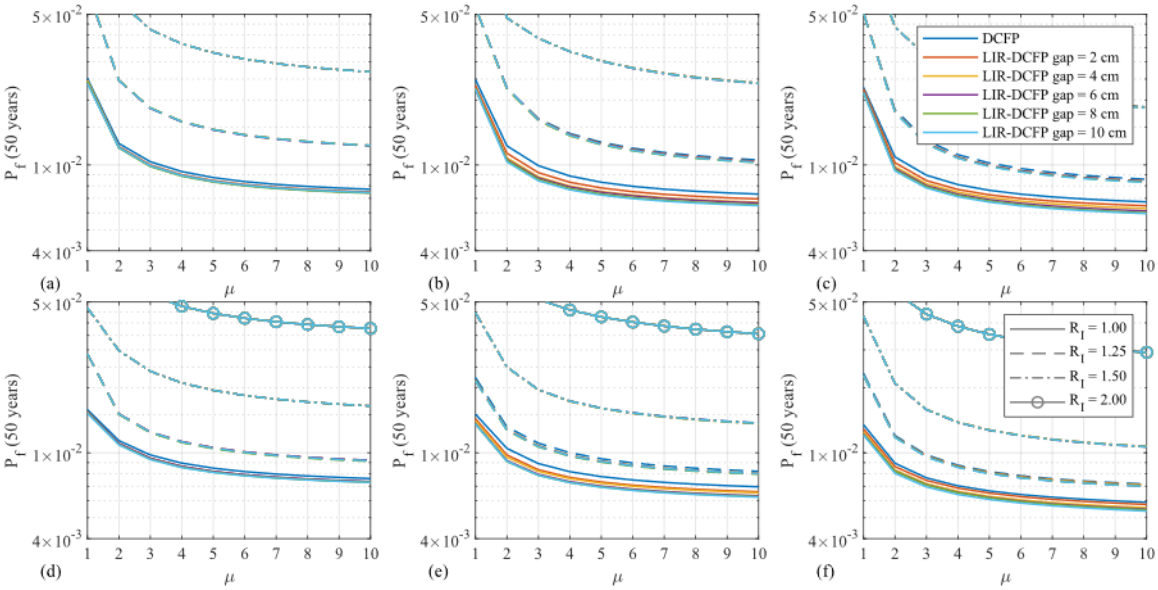

Figure 23: Seismic reliability of the superstructure for $T_b = 5$ sec and $r_S = -0.10$: (a) $\gamma = 0.7$ and $T_s = 0.3$ sec; (b) $\gamma = 0.7$ and $T_s = 0.6$ sec; (c) $\gamma = 0.7$ and $T_s = 0.9$ sec; (d) $\gamma = 0.9$ and $T_s = 0.3$ sec; (e) $\gamma = 0.9$ and $T_s = 0.6$ sec; (f) $\gamma = 0.9$ and $T_s = 0.9$ sec.

Considering cases with hardening behavior and $R_I = 1.00$, the improvement in the seismic performance using LIR-DCFP bearings is highlighted for low values of T_s, low values of γ and high values of r_H (Figure 24). By using LIR-DCFP bearings with internal gaps of 10 cm reduction in the probabilities of exceeding LSs_μ up to 20% are achievable (Figure 24(a)). This result is coherent with the fragility curves and several studies indicating that stiff base-isolated superstructures (e.g., concentrically braced steel frames and non-slender reinforce concrete buildings) are very sensitive to impact forces [15–17]. Hence, using LIR-DCFP bearing is very attractive to improve the seismic performance of stiff base-isolated structures. The improvement in the seismic performance is noticeable even for cases with $R_I = 1.25$ and superstructures characterized, especially, by a hardening behavior (Figure 25). This better performance is highlighted for stiff structures (i.e., $T_s = 3$ sec) and a relatively high post-yield ratio ($r_H = 0.10$). In Figure 25((a), (b), (e), and (f)), these cases are plotted using red and blue dashed lines.

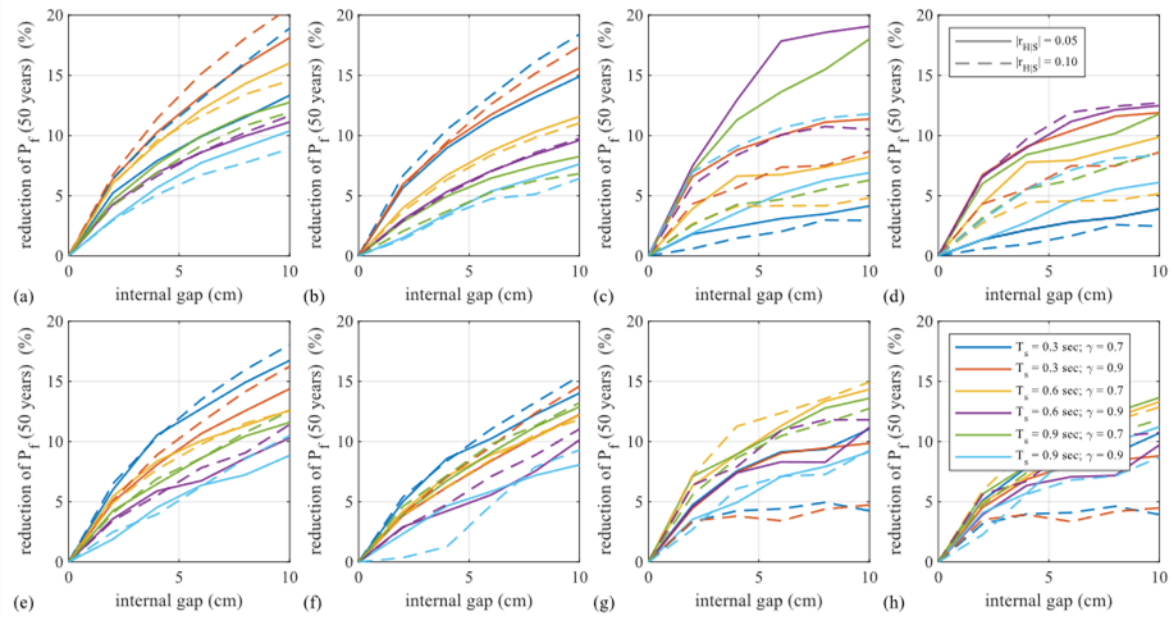

Figure 24: Reduction of the ductility demand for increasing values of internal gap of LIR-DCFP bearings for $R_I = 1.0$: (a) Hardening $LS_\mu = 3$ and $T_b = 3$ sec; (b) Hardening $LS_\mu = 5$ and $T_b = 3$ sec; (c) Softening $LS_\mu = 3$ and $T_b = 3$ sec; (d) Softening $LS_\mu = 5$ and $T_b = 3$ sec; (e) Hardening $LS_\mu = 3$ and $T_b = 5$ sec; (f) Hardening $LS_\mu = 5$ and $T_b = 5$ sec; (g) Softening $LS_\mu = 3$ and $T_b = 5$ sec; (h) Softening $LS_\mu = 5$ and $T_b = 5$ sec.

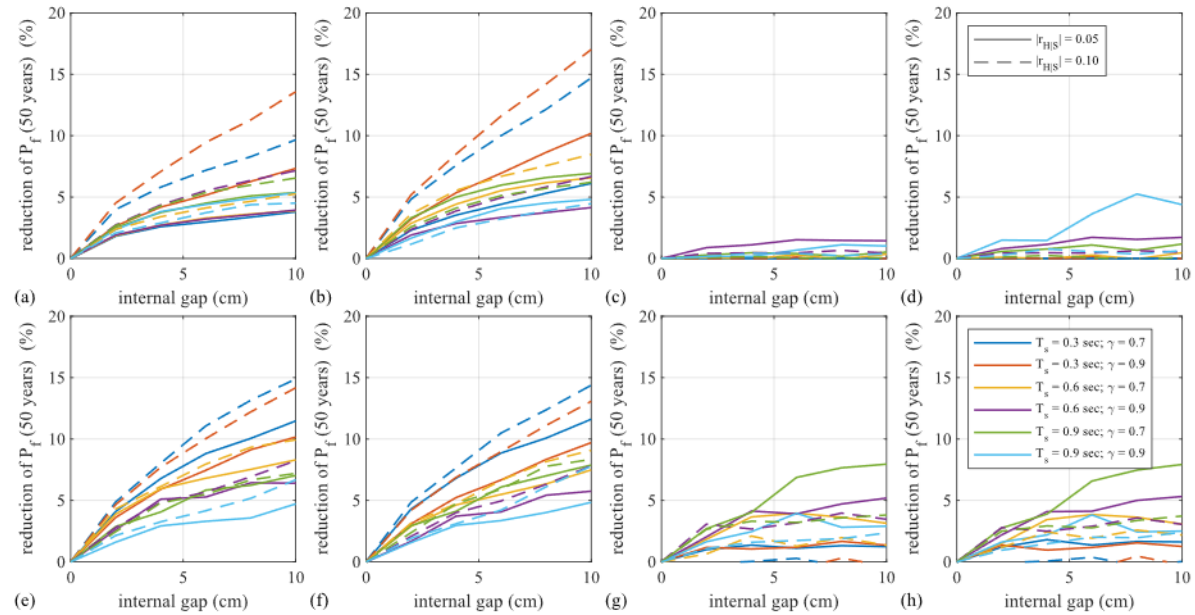

Figure 25: Reduction of the ductility demand for increasing values of internal gap of LIR-DCFP bearings for softening cases and $R_I = 1.25$: (a) Hardening $LS_\mu = 3$ and $T_b = 3$ sec; (b) Hardening $LS_\mu = 5$ and $T_b = 3$ sec; (c) Softening $LS_\mu = 3$ and $T_b = 3$ sec; (d) Softening $LS_\mu = 5$ and $T_b = 3$ sec; (e) Hardening $LS_\mu = 3$ and $T_b = 5$ sec; (f) Hardening $LS_\mu = 5$ and $T_b = 5$ sec; (g) Softening $LS_\mu = 3$ and $T_b = 5$ sec; (h) Softening $LS_\mu = 5$ and $T_b = 5$ sec.

The results obtained considering cases sensitive to $P - \Delta$ effects also present important reductions in the probability of exceedance $LS_\mu = 3$ and $LS_\mu = 5$. Not negligible benefits of using LIR-DCFP bearings are achieved also for the rise of the parameter R_I in cases of structures characterized by softening behavior, particularly, for low absolute values of the post-yield ratio (i.e., $|r_S| = 0.05$).

9. Conclusions

This paper describes the seismic reliability-based performance of nonlinear structures seismically isolated using frictional devices, highlighting the scenarios in which using Lateral Impact Double Concave Friction Pendulum (LIR-DCFP) bearings is recommended over DCFP bearings having the same size for both the plates and slider. This novel seismic isolator has been proposed as a solution to problems generated by the internal impact between the inner slider and the restraining rims of the isolators: the failure of this type of bearings and the dramatic rise in the ductility demand generated by internal lateral impacts. Within a wide parametric analysis, several elastic and inelastic properties of the superstructure and isolation system were considered, assuming the friction coefficients and characteristics of the seismic inputs as the relevant random variables. The superstructure was characterized by a 1dof system, exhibiting nonlinear behavior in the lateral direction. The post-yield stiffness of the superstructure was considered having hardening or softening post-yield lateral stiffness (not sensitive or sensitive to $P-\Delta$ effects). The isolation system was modeled using a rigid body approach that allows, among other physical phenomena, including the internal lateral impact behavior. A comparison between two frictional isolators were considered in the analysis: non-articulated DCFP and LIR-DCFP bearings. The lateral capacity of the isolation system and the inelastic properties of the superstructure were designed according to the criteria of the ASCE/SEI 7-16 standard.

For each considered isolated period, ten sets of 30 natural records scaled to match Conditional Spectra of a site in Riverside (California) were selected. Incremental Dynamic Analyses were performed to determine the statistics of the maximum base displacement of the upper sliding surface and ductility demand of the superstructure. The results of the IDAs were used to construct the seismic fragility curves related to different limit state thresholds. Finally, the seismic reliability curves of 1,152 equivalent seismically isolated systems equipped with DCFP or LIR-DCFP bearings, in a time frame of 50 years, were constructed. These curves were valuable to compare the seismic performance of the DCFP and LIR-DCFP devices with important design suggestions for the superstructure and internal gap.

In the studied cases with hardening post-yield stiffness (equipped with DCFP or LIR-DCFP bearings), an increment in the post-yield ratio leads to better seismic performance in terms of ductility demand thresholds. The opposite happens if softening behavior is exhibited. An increment in the absolute value of the post-yield softening stiffness generates a reduction of the seismic reliability. In cases in which the superstructure is designed to behave essentially elastic if the internal lateral capacity is not reached, better seismic performance is achieved using LIR-DCFP bearings. In these cases, an increment in the internal gap of the LIR-DCFP bearing, increasing the additional energy dissipation capacity and limiting the magnitude of impact forces, reduces the probabilities exceeding ductility demands thresholds. Considering superstructures with hardening post-yield behavior, the benefits of using the proposed seismic isolator are highlighted, especially, for low values of the period of the superstructure and low values of the mass distribution ratios. In the cases in which the yielding of the superstructure is allowed before the occurrence of the internal lateral impact, using LIR-DCFP bearings is recommended if the superstructure is stiff and has a relatively high post-yield hardening stiffness. In cases with softening behavior, the adverse effects of internal impacts are mitigated if the superstructure is designed to remain essentially elastic before the occurrence of the impact. However, not negligible benefits are achieved also for superstructures designed to exhibit the nonlinear softening behavior before the occurrence of the internal impact combined with low absolute values of the post-yield ratios. In cases in which the nonlinear behavior of the superstructure is exhibited before the occurrence of the lateral impact, the benefits of using the novel seismic isolator are reduced.

In general, better seismic performance is quite always achieved using LIR-DCFP bearings reaching reduction up to 20% in the probabilities exceeding ductility demand thresholds in a time frame of 50 years. These advantages derive from the presence of the internal gap with infinite curvature combined with the higher friction coefficient and are not necessarily achievable by increasing the size of classical DCFP devices.

Acknowledgements

This research has been funded by the National Agency for Research and Development (ANID) through the ANID-PCHA/Doctorado Nacional/2018-21180434 and the FONDECYT project N◦1201841, the authors are grateful for the support.

References

[1] J.M. Kelly, Earthquake-Resistant Design with Rubber, 1st ed., Springer London, London, 1993.

[2] V.A. Zayas, S.S. Low, S.A. Mahin, A Simple Pendulum Technique for Achieving Seismic Isolation, Earthq. Spectra. 6 (1990) 317–333. https://doi.org/10.1193/1.1585573.

[3] A. Mokha, M. Constantinou, A. Reinhorn, Teflon Bearings in Base Isolation I: Testing, J. Struct. Eng. 116 (1990) 438–454. https://doi.org/10.1061/(ASCE)0733-9445(1990)116:2(438).
[4] M. Constantinou, A. Mokha, A. Reinhorn, Teflon Bearings in Base Isolation II: Modeling, J. Struct. Eng. (2007). https://doi.org/10.1061/(asce)0733-9445(1990)116:2(455).
[5] D.M. Fenz, M.C. Constantinou, Spherical sliding isolation bearings with adaptive behavior: Experimental verification, Earthq. Eng. Struct. Dyn. 37 (2008) 185–205. https://doi.org/10.1002/eqe.750.
[6] D.M. Fenz, M.C. Constantinou, Behaviour of the double concave Friction Pendulum bearing, Earthq. Eng. Struct. Dyn. 35 (2006) 1403–1424. https://doi.org/10.1002/eqe.589.
[7] D.M. Fenz, M.C. Constantinou, Spherical sliding isolation bearings with adaptive behavior: Theory, Earthq. Eng. Struct. Dyn. 37 (2008) 163–183. https://doi.org/10.1002/eqe.751.
[8] D.M. Fenz, M.C. Constantinou, Modeling triple friction pendulum bearings for response-history analysis, Earthq. Spectra. 24 (2008) 1011–1028. https://doi.org/10.1193/1.2982531.
[9] R.S. Jangid, J.M. Kelly, Base isolation for near-fault motions, Earthq. Eng. Struct. Dyn. 30 (2001) 691–707.
[10] J.F. Hall, T.H. Heaton, M.W. Halling, D.J. Wald, Near-Source Ground Motion and its Effects on Flexible Buildings, Earthq. Spectra. 11 (1995) 569–605. https://doi.org/10.1193/1.1585828.
[11] F. Mazza, A. Vulcano, Effects of near-fault ground motions on the nonlinear dynamic response of base-isolated r.c. framed buildings, Earthq. Eng. Struct. Dyn. 41 (2012) 211–232. https://doi.org/10.1002/eqe.1126.
[12] F. Mazza, Seismic demand of base-isolated irregular structures subjected to pulse-type earthquakes, Soil Dyn. Earthq. Eng. 108 (2018) 111–129. https://doi.org/10.1016/j.soildyn.2017.11.030.
[13] Y. Bao, T.C. Becker, H. Hamaguchi, Failure of double friction pendulum bearings under pulse-type motions, Earthq. Eng. Struct. Dyn. 46 (2017) 715–732. https://doi.org/10.1002/eqe.2827.
[14] T.C. Becker, Y. Bao, S.A. Mahin, Extreme behavior in a triple friction pendulum isolated frame, Earthq. Eng. Struct. Dyn. 46 (2017) 2683–2698. https://doi.org/10.1002/eqe.2924.
[15] Y. Bao, T.C. Becker, Inelastic response of base-isolated structures subjected to impact, Eng. Struct. 171 (2018) 86–93. https://doi.org/10.1016/j.engstruct.2018.05.091.
[16] Y. Bao, T.C. Becker, T. Sone, H. Hamaguchi, To limit forces or displacements: Collapse study of steel frames isolated by sliding bearings with and without restraining rims, Soil Dyn. Earthq. Eng. 112 (2018) 203–214.
[17] Y. Bao, T.C. Becker, Effect of Design Methodology on Collapse of Friction Pendulum Isolated Moment-Resisting and Concentrically Braced Frames, J. Struct. Eng. 144 (2018) 04018203.
[18] E.A. Mavronicola, P.C. Polycarpou, P. Komodromos, Spatial seismic modeling of base-isolated buildings pounding against moat walls : effects of ground motion directionality and mass eccentricity, (2017) 1161–1179. https://doi.org/10.1002/eqe.
[19] P.C. Polycarpou, P. Komodromos, Earthquake-induced poundings of a seismically isolated building with adjacent structures, Eng. Struct. 32 (2010) 1937–1951. https://doi.org/10.1016/j.engstruct.2010.03.011.
[20] P. Komodromos, Simulation of the earthquake-induced pounding of seismically isolated buildings, Comput. Struct. 86 (2008) 618–626. https://doi.org/10.1016/j.compstruc.2007.08.001.
[21] G. Auad, J.L. Almazán, Lateral Impact Resilient double concave Friction Pendulum (LIR-DCFP) bearing: Formulation, parametric study of the slider and three-dimensional numerical example, Eng. Struct. 233 (2021).
[22] P. Castaldo, E. Tubaldi, Influence of FPS bearing properties on the seismic performance of base-isolated structures, Earthq. Eng. Struct. Dyn. 44 (2015) 2817–2836. https://doi.org/10.1002/eqe.2610.
[23] P. Castaldo, G. Amendola, B. Palazzo, Seismic fragility and reliability of structures isolated by friction pendulum devices: seismic reliability-based design (SRBD), Earthq. Eng. Struct. Dyn. 46 (2017) 425–446.
[24] P. Castaldo, M. Ripani, Optimal design of friction pendulum system properties for isolated structures considering different soil conditions, Soil Dyn. Earthq. Eng. 90 (2016) 74–87.
[25] P. Castaldo, B. Palazzo, G. Alfano, M.F. Palumbo, Seismic reliability-based ductility demand for hardening and softening structures isolated by friction pendulum bearings, Struct. Control Heal. Monit. 25 (2018) 2256.
[26] P. Castaldo, B. Palazzo, T. Ferrentino, Seismic reliability-based ductility demand evaluation for inelastic base-isolated structures with friction pendulum devices, Earthq. Eng. Struct. Dyn. 46 (2017) 1245–1266.
[27] P. Castaldo, B. Palazzo, P. Della Vecchia, Seismic reliability of base-isolated structures with friction pendulum bearings, Eng. Struct. 95 (2015) 80–93. https://doi.org/10.1016/j.engstruct.2015.03.053.
[28] P. Castaldo, B. Palazzo, P. Della Vecchia, Life-cycle cost and seismic reliability analysis of 3D systems equipped with FPS for different isolation degrees, Eng. Struct. 125 (2016) 349–363.
[29] S. Kitayama, M.C. Constantinou, Probabilistic seismic performance assessment of seismically isolated buildings designed by the procedures of ASCE/SEI 7 and other enhanced criteria, Eng. Struct. 179 (2019) 566–582. https://doi.org/10.1016/J.ENGSTRUCT.2018.11.014.
[30] S. Kitayama, M.C. Constantinou, Effect of displacement restraint on the collapse performance of seismically

isolated buildings, Bull. Earthq. Eng. 2019 175. 17 (2019) 2767–2786. https://doi.org/10.1007/S10518-019-00554-Y.
[31] ASCE, Minimum Design Loads and Associated Criteria for Buildings and Other Structures, ASCE/SEI 7-16. (2016).
[32] Y. Bao, T. Becker, Three-dimensional double friction pendulum bearing model including uplift and impact behavior: Formulation and numerical example, Eng. Struct. 199 (2019) 109579.
[33] T. Lin, C.B. Haselton, J.W. Baker, Conditional spectrum-based ground motion selection. Part I: Hazard consistency for risk-based assessments, Earthq. Eng. Struct. Dyn. 42 (2013) 1847–1865.
[34] J.W. Baker, C. Lee, An Improved Algorithm for Selecting Ground Motions to Match a Conditional Spectrum, J. Earthq. Eng. 22 (2018) 708–723. https://doi.org/10.1080/13632469.2016.1264334.
[35] T. Lin, C.B. Haselton, J.W. Baker, Conditional spectrum-based ground motion selection. Part II: Intensity-based assessments and evaluation of alternative target spectra, Earthq. Eng. Struct. Dyn. 42 (2013) 1867–1884. https://doi.org/10.1002/eqe.2303.
[36] T. Lin, C.B. Haselton, J.W. Baker, Conditional spectrum-based ground motion selection. Part I: Hazard consistency for risk-based assessments, Earthq. Eng. Struct. Dyn. 42 (2013) 1847–1865.
[37] B.R. Hunt, R.L. Lipsman, J.M. Rosenberg, K.R. Coombes, J.E. Osborn, G.J. Stuck, A Guide to MATLAB ® , 2006. https://doi.org/10.1017/cbo9780511791284.
[38] Y.J. Park, Y.K. Wen, A.H.-S. Ang, Random vibration of hysteretic systems under bi-directional ground motions, Earthq. Eng. Struct. Dyn. 14 (1986) 543–557. https://doi.org/10.1002/eqe.4290140405.
[39] F. Naeim, J. Kelly, Design of seismic isolated structures: from theory to practice, (1999).
[40] Y.K. Wen, Method for Random Vibration of Hysteretic Systems, ASCE J Eng Mech Div. 102 (1976) 249–263. https://doi.org/10.1061/jmcea3.0002106.
[41] A.K. Chopra, Dynamics of Structures: Theory and Applications to Earthquake Engineering, Prentice Hall, 1995. https://doi.org/10.1193/1.2720354.
[42] P.E.E.R.C. PEER, PEER Ground Motion Database, Shallow Crustal Earthquakes Act. Tecton. Regimes, NGA-West2. (2013).
[43] B. Palazzo, Seismic behavior of base isolated buildings, in: Int. Meet. Earthq. Prot. Build. Ancona, 1991.
[44] A. Gupta, Seismic demands for performance evaluation of steel moment resisting frame structures, Stanford University, 1999.
[45] C. Adam, L.F. Ibarra, H. Krawinkler, Evaluation of P-delta effects in non-deteriorating MDOF structures from equivalent SDOF systems, in: 13th World Conf. Earthq. Eng., 2004.
[46] P. Castaldo, G. Alfano, Seismic reliability-based design of hardening and softening structures isolated by double concave sliding devices, Soil Dyn. Earthq. Eng. 129 (2020) 105930.
[47] M.D. McKay, R.J. Beckman, W.J. Conover, A comparison of three methods for selecting values of input variables in the analysis of output from a computer code, Technometrics. 42 (2000) 55–61.
[48] M. Vořechovský, D. Novák, Correlation control in small-sample Monte Carlo type simulations I: A simulated annealing approach, Probabilistic Eng. Mech. 24 (2009) 452–462.
[49] Unified Hazard Tool, (n.d.). https://earthquake.usgs.gov/hazards/interactive/ (accessed June 17, 2021).
[50] J.W. Baker, Conditional Mean Spectrum: Tool for Ground-Motion Selection, J. Struct. Eng. 137 (2011) 322–331. https://doi.org/10.1061/(asce)st.1943-541x.0000215.
[51] D.M. Boore, J.P. Stewart, E. Seyhan, G.M. Atkinson, NGA-West2 equations for predicting PGA, PGV, and 5% damped PSA for shallow crustal earthquakes, Earthq. Spectra. 30 (2014) 1057–1085.
[52] J.W. Baker, N. Jayaram, Correlation of spectral acceleration values from NGA ground motion models, Earthq. Spectra. 24 (2008) 299–317. https://doi.org/10.1193/1.2857544.
[53] M. Kikuchi, C.J. Black, I.D. Aiken, On the response of yielding seismically isolated structures, Earthq. Eng. Struct. Dyn. 37 (2008) 659–679. https://doi.org/10.1002/eqe.777.
[54] M.F. Vassiliou, A. Tsiavos, B. Stojadinović, Dynamics of inelastic base-isolated structures subjected to analytical pulse ground motions, Earthq. Eng. Struct. Dyn. 42 (2013) 2043–2060.
[55] A. Tsiavos, T. Markic, D. Schlatter, B. Stojadinovic, Shaking table investigation of inelastic deformation demand for a structure isolated using friction-pendulum sliding bearings, Structures. 31 (2021) 1041–1052.
[56] P. Bazzurro, A. Cornell, Z. Member, N. Asce, / Shome, J.E. Carballo, Three proposals for characterizing MDOF nonlinear seismic response, (n.d.).